Design and Numerical Analysis of an Unconventional Surface-Piercing Propeller for Improved Performance at Low and High Speeds

by

Justin Richard Parker

B.S. Aerospace Engineering, University of Maryland (2008)

Submitted to the Department of Mechanical Engineering
in partial fulfillment of the requirements for the degrees of

Naval Engineer

and

Master of Science in Mechanical Engineering

at the

MASSACHUSETTS INSTITUTE OF TECHNOLOGY

June 2017

Author ..... Signature redacted .....
Department of Mechanical Engineering
May 12, 2017

Certified by... Signature redacted .....
Stefano Brizzolara
Associate Professor of Ship Dynamics, Virginia Tech
Thesis Supervisor

Certified by... Signature redacted .....
Michael S. Triantafyllou
Professor of Mechanical and Ocean Engineering
Thesis Supervisor

Accepted by ..... Signature redacted .....
Rohan Abeyaratne
Chairman, Department Committee on Graduate Students

Design and Numerical Analysis of an Unconventional Surface-Piercing Propeller for Improved Performance at Low and High Speeds

by

Justin Richard Parker

Submitted to the Department of Mechanical Engineering
on May 12, 2017, in partial fulfillment of the
requirements for the degrees of
Naval Engineer
and
Master of Science in Mechanical Engineering

Abstract

Traditional propellers operate fully submerged, with cavitation limited as much as possible in order to minimize its disruptive and damaging consequences. Conversely, supercavitating propellers operate in an encompassing vapor cavity, thereby averting these negative effects while substantially reducing drag on the blades. Surface-piercing propellers, operating under a similar concept as supercavitation, often achieve even greater efficiency by drawing in an air cavity from the free surface. Existing small craft have demonstrated the ability of such propellers to yield extremely high speeds (110+ knots); nevertheless, the full potential of these propellers has yet to be explored. In particular, designs often neglect low-speed performance, focusing solely on high-speed operation. This research therefore developed a new surface-piercing propeller concept designed instead to maximize performance across the spectrum of operating speeds.

Applying established theory for supercavitating hydrofoils, the new blades were shaped based on theoretical maximally-efficient two-dimensional profile sections. Furthermore, in order to affect the low-speed performance enhancement, the trailing edge of each profile was appended with a unique "tail" form that allows the blade to resemble a traditional propeller when operating at subcavitating speeds without sacrificing supercavitating performance. The design used an existing racing propeller as a baseline for comparison, matching certain characteristics (rotational speed, advance speed, number of blades, hub size) in order to ensure equivalent operating conditions. Computational fluid dynamics (CFD) of the 2D profiles informed changes to the profile shapes until lift-to-drag (L/D) was maximized while ensuring a fully-encompassing vapor cavity. The complete propeller was drafted from these optimized radial sections for full 3D CFD analysis.

Results from both the 2D and 3D CFD simulations revealed promising benefits to propulsive efficiency. High-speed performance met or exceeded that of the baseline propeller, and low-speed performance showed significant improvement. This surface-piercing propeller concept offers an unconventional design with convincing results for balanced low- and high-speed operation.

Thesis Supervisor: Stefano Brizzolara
Title: Associate Professor of Ship Dynamics, Virginia Tech

Thesis Supervisor: Michael S. Triantafyllou
Title: Professor of Mechanical and Ocean Engineering

Acknowledgments

I would like to thank Professor **Stefano Brizzolara** not only for his support and guidance in this thesis project but moreover for his inspiration throughout my graduate education. From the first lecture he gave in 2.701 Introduction to Naval Architecture nearly three years ago, his passion for his work shone through as clearly as his superior knowledge and expertise in the subject. This passion was infectious, and I was instantly captivated by the field of high-speed hydrodynamics. Soon after agreeing upon a thesis topic, I discovered that not only was Professor Brizzolara's dedication to his field exceptional but so too was his dedication to his students. Always taking the time to thoroughly explain complicated concepts (in the simplest terms when necessary) and providing significant thesis guidance from start to finish, he ensured that I grasped both the underlying theories as well as the analytical procedures in order to conduct substantive research. My only regret is that he left MIT for Virginia Tech! Nevertheless, Professor Brizzolara, I wish you all the best in your already highly-accomplished career.

I would also like to thank **John Scherer** of Mercury Marine, who generously contributed his propeller data for the design and analyses in this thesis. In addition, he was always prompt to reply with further details, or even a hand-drawn diagram to help explain propeller concepts. Dr. Scherer, thank you for all your support!

Of course I must thank my parents, **Drs. Soon Park and Richard Parker**, not only for their love and support throughout my entire life but in particular for their inspiration in higher education. As a graduate college professor herself, my mom continues to motivate me to be the best student possible (and thus has often been that voice in my head telling me to "stop procrastinating!") and to always push myself to learn more, study harder, absorb knowledge at every opportunity. As a medical doctor, my dad has demonstrated the significant impact of higher education throughout his accomplished career. The success of both my parents in their professions will forever inspire me to achieve my own success through hard work and the continual pursuit of knowledge.

Above all, I would like to thank my wife, **Joanna Parker**, for her boundless support throughout my graduate education. Through all the long days at school, stressful weekends before exams and deadlines, and of course the occasional all-nighter, she rose to the challenge of meeting my stress head-on with a limitless supply of love and care (and absolutely delicious home-cooked meals to fuel the brain). In the particularly frenetic final month of completing this thesis, she again demonstrated that I am the luckiest man in the world to have her as my wife. Joanna, no words can capture how appreciative I am of everything you have done for me. I am forever thankful for you, and none of the work contained in this thesis would have been possible without you. Thank you. I love you so much!

THIS PAGE INTENTIONALLY LEFT BLANK

Contents

List of Figures

List of Tables

List of Symbols

C	Blade Section Chord [m]
c	Distance Along Blade Section Chord [m]
C_D	Blade Section Drag Coefficient
C_L	Blade Section Lift Coefficient
D	Drag [N]
d	Propeller Diameter [m]
I_2	Area Principal Moment of Inertia [m^4]
J	Propeller Advance Ratio
K_Q	Propeller Torque Coefficient
K_T	Propeller Thrust Coefficient
L	Lift [N]
$\dot{m}$	Mass Flow Rate [kg/s]
N	Number of Propeller Blades
n	Propeller Rotative Speed [Hz]
P	Pressure [Pa]
Q	Torque [N-m]
R	Propeller Radius [meters]
r	Distance Along Propeller Radius [m]
R_e	Reynold's Number
S	Section Modulus [m^3]
t	Thickness [m] (or *time* if used in conjunction with a derivative)
T	Thrust [N]
T_{Re}	Tensor of Reynolds Stresses [N]
V	Velocity [m/s]
V_a	Speed of Advance (freestream velocity) [m/s]
α	Angle of Attack [deg]

α_{phase}	Phase concentration (where *phase* is liquid, vapor, or air)
β	Inflow Angle [deg]
η_p	Open-Water Propeller Efficiency
μ	Dynamic Viscosity [Pa-s]
ν	Kinematic Viscosity [m^2/s]
Ω	Vorticity [Hz]
φ	Pitch Angle [deg]
ρ	Density [kg/m^3]
σ	Cavitation Number
θ	Parameter defining distance along hydrofoil chord

Chapter 1

Background

Traditional propellers operate fully submerged, at relatively low speeds, with cavitation effects limited as much as possible. This report instead explores a partially-submerged, high-speed propeller optimized for operation in a fully-cavitated state. By harnessing the benefits of supercavitating hydrofoil design combined with surface-piercing operation, this unconventional propeller aims to achieve significant hydrodynamic efficiency for high-speed watercraft. Furthermore, the design specifically targets increased efficiency in the low speed regime - an area generally neglected in high-speed propeller design - without sacrificing overall performance.

An overview of cavitation is presented, noting how it is a phenomenon to be avoided in marine engineering. On the contrary, *super*cavitation offers significant hydrodynamic advantages while avoiding the unfavorable effects of cavitation; it is discussed in general here, and its applicable theory is presented in greater detail in Chapter 2. We then present two unique features to the propeller of this report: surface-piercing operation and an exclusive hydrofoil trailing edge design known as *SCSB*.

1.1 Cavitation and Its Damaging Effects

Cavitation, in general, is an extremely undesirable phenomenon in marine applications. Resulting from local fluid pressure dropping below the vapor pressure of the liquid, cavitation is the formation of vapor cavities that serve to disrupt the flow around them. These bubbles are both quick to form and quick to implode, causing shock to the body. Although generally small and localized, these implosions can add up to induce significant detriments to the system, such as:

- **Flow disturbance**, causing undesireable changes in the hydrodynamic properties (i.e. a reduction in lift);
- **Mechanical vibrations**, which can cause hydro-acoustic noise and system wear;
- **Material damage**, in the form of surface erosion [25].

Figure 1-1: The pitfalls of cavitation: propellers showing significant pitting damage [29]

For example, cavitation is notoriously the cause of pitting damage on propellers, where the surfaces of the propeller blades become covered in pits where pockets of material have eroded. Eventually, this damage can become so severe as to render the propellers unusable, as shown on the discarded blades of Figure 1-1. All of these negative consequences lead marine engineering textbooks to advise "designing and operating... to avoid cavitation and its adverse effects on performance" [25].

Cavitation as related to marine propulsion was first scientifically observed in 1894 by Sir Charles Parson in the United Kingdom. He built the first cavitation tunnel to study the causes and effects of cavitation on propellers. His research led to changes in propeller design that created successful noncavitating propulsors capable of avoiding the negative effects of cavitation. However, such designs imposed limitations on speed; attempts to use these

designs on higher-speed vessels once again brought about damaging consequences. The interwar German Navy, for example, applied noncavitating propeller designs to fast destroyers and torpedo boats, and the result was that "in 200 hours of full-speed cruising the indicated screw propellers would acquire such a damage (erosion blisters of size of a fist)... that their replacement became inevitable" [1]. To effect higher speeds without such devastating effects, a new approach was required.

1.2 Supercavitation and Its Application to Propellers

When applied in a certain manner, cavitation can in fact be harnessed to gain hydrodynamic advantages. Specifically, the application of *super*cavitation can precipitate significant advances in maritime speed and efficiency. Whereas "cavitation" refers generally to the development of vapor bubbles on a submerged body to rapid pressure changes, "supercavitation" signifies that those individual cavities have been replaced by a single large cavity that envelopes an entire surface. This cavity is sufficiently strong so as to avoid collapsing around the body, instead delaying the collapse until it is harmlessly far downstream. In this way, the body is not subject to the repeated implosions that are the cause of so many detrimental effects on submerged bodies.

By reaching the supercavitating stage, not only is cavitation damage avoided but furthermore considerable hydrodynamic efficiency may be gained. With a substantial portion of the submerged body covered in a vapor cavity, drag on that body is *significantly* reduced. Owing to the lower viscosity of vapor as compared to liquid, the submerged body encounters considerably less resistance in the encompassing cavity. It is therefore possible to achieve drastically higher speeds with a body designed to achieve supercavitation than with a body designed to avoid it.

Systematic analysis of propellers designed to leverage rather than avoid cavitation began in 1941 under the Russian scientist Valentin Lvovich Pozdunin. He designed and tested propellers that operated in the supercavitating regime, proving that erosion could be avoided with a sufficiently strong cavity that avoided collapse until far enough downstream of the blade. His research, however, revealed several challenges with supercavitating blade design:

- **Structural strength**: supercavitating profiles must have thin leading edges, which may lead to insufficient local strength of the blade on a full-size propeller;
- **Cavity strength**: at full cruising speed, the cavity must have sufficient length and thickness so as to withstand fluctuations without any local collapse;
- **Profile shape**: in order to purely optimize supercavitation, the ideal profile shape is a wedge, rather than the traditional hydrofoil profile; while ideal for supercavitation, this shape is not optimal for overall hydrodynamic performance;

- **Subcavitating performance**: in order to overcome the "cavitation barrier" (i.e. before sustained supercavitation is achieved), the propulsor must be able to produce sufficient thrust at lower speeds in the subcavitating regime [1].

These points became areas of critical emphasis for all supercavitating designs, and accordingly they are each addressed for the propeller of this report.

Despite the challenges associated with supercavitating propellers, their efficacy has been repeatedly demonstrated in the decades since Pozdunin. American research in the subject began in the 1950s at the U.S. Navy David Taylor Model Basin, resulting in a wealth of model tests confirming theoretical predictions. The following decade the Canadian navy applied supercavitating propellers to their *Bras d'Or* hydrofoil ship, evidencing the capability of these propellers to drive the 235-ton craft to speeds in excess of 60 knots [10] [1]. Today, while many high-speed boats have turned to waterjet propulsion, supercavitating propellers nevertheless continue to find substantial employment in a multitude of fast watercraft. The Juliet Marine *Ghost* (Figure 1-2), an advanced submerged waterplane twin hull (SWATH) naval prototype, is one recent example of a craft employing supercavitating propellers to achieve efficient high speeds [16].

Figure 1-2: *Ghost* naval prototype craft featuring supercavitating propellers [16]

1.3 The Surface-Piercing Advantage

As Pozdunin discovered, supercavitating propeller designs must deal with several challenging criteria to ensure that the blades are effective at leveraging the benefits of supercavitation. To guarantee cavity initiation and sustainment, the submerged body must attain high speeds and have a sharp leading edge in order to develop sufficient pressure differential. Once sustained, the cavity will allow the body to operate efficiently at high speed, however the power required to overcome this "cavitation barrier" may offset gains in operational efficiency. The characteristics of *surface-piercing* propellers offer the potential to mitigate these transient challenges while still reaping the benefits of supercavitating hydrodynamics.

Surface-piercing propellers work under the same general concept as supercavitating propellers: to operate in an enveloping cavity so as to avoid the negative effects of cavitation, and in doing so achieving superior efficiency by way of significantly reduced drag. The difference is that whereas supercavitating propellers rely on a substantial pressure differential to instigate cavitation, surface-piercing propellers exploit the air above the free surface to mimic cavitation. These propellers sit partially submerged, with generally only one-third of the diameter below the surface. Therefore, with each rotation, air is drawn in with the blades. The result is an air cavity surrounding the blades - that is, *ventilation* rather than *cavitation*. Consequently, several distinct advantages may be realized over their submerged counterparts:

- Supercavitation benefits can be gained from nearly the onset of rotation, owing to the air cavity being pulled in straight from the free surface rather than requiring sufficient rotative speed to develop a pressure differential;
- Appendage drag is reduced, as the propulsion gear is elevated out of the water;
- Propeller draft below the keel is minimized, supporting shallow-water operations [38].

The two conditions of *ventilation* and *cavitation* and their overall hydrodynamic effects however are generally the same, and as such the terms may be used interchangeably when discussing surface-piercing propellers [25]. Moreover, due to the similarity of the phenomena, surface-piercing propellers benefit from the same design

Figure 1-4: Fountain *Lighting* racing craft featuring Mercury surface-piercing propellers [32]

considerations as for supercavitating propellers. This report's design therefore seeks to leverage the advantages of both supercavitating and surface-piercing concepts.

Surface-piercing propellers are employed on a number of high-speed racing craft, such as the Fountain *Lighting* (Figure 1-4). This craft sports four Mercury Marine supercavitating propellers which allow the vessel to achieve speeds in excess of 100 knots. These Mercury propellers form the baseline for design and comparison of this report's concept propeller.

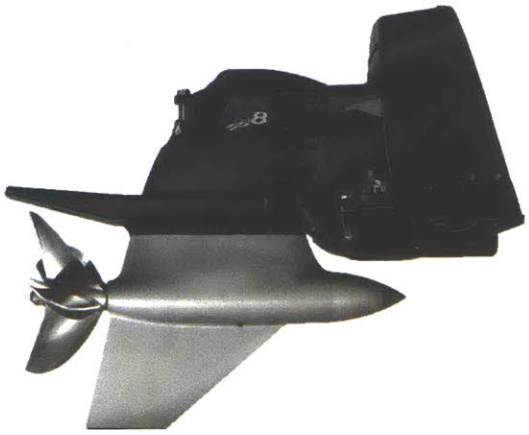

Figure 1-3: Mercury Racing M8 inboard drive with surface-piercing propeller [32]

In addition to the benefits, surface-piercing propellers also come with their own unique set of challenges. Many of the challenges relate to propeller/hull interaction issues, such as the need to manage the higher lateral forces and moments [28]. However, as the propeller of this research is based on an existing design that already been proven in operation, such challenges are not considered in this report. The research here instead focuses purely on the development and open-water comparison of the propellers themselves, rather than taking into account secondary boat interface effects.

1.4 The *SCSB* Hydrofoil

Throughout the development of supercavitating and surface-piercing propeller design, the focus has remained predominantly on high-speed effectiveness. Little attention has been given to low-speed performance, an important regime not only for general transit efficiency (for example, transiting in and out of harbors) but also for achieving rapid acceleration to full cavitation speeds. Dr. Stefano Brizzolara of MIT sought to address this issue in 2015 with the development of a new family of hydrofoils, termed *SCSB*. These foils combined a traditional supercavitating profile with the advent of a new "tail" design, as illustrated in Figure 1-5. The tail, shown in blue, exists entirely in the vapor cavity when at fully cavitating speeds and therefore does not impede the foil's supercavitating performance. At lower, subcavitating speeds, however, the tail induces markedly improved performance. Whereas the traditional blunt trailing edge causes significant vortex drag, the tail not only offsets this energy loss but also provides a number of additional benefits. The key advantages of the SCSB profile include:

- Increased lift by adding effective camber;
- Reduced pressure drag by eliminating the blunt trailing edge;
- Improved strength by increasing the foil's sectional area and inertia modulus [5].

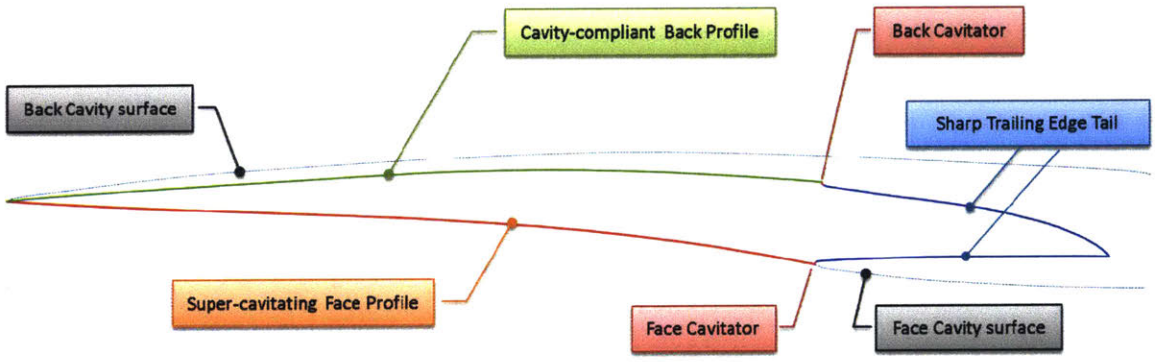

Figure 1-5: Principal topological elements of the SCSB hydrofoil [5]

Numerical analysis of 2D hydrofoil profiles has demonstrated that the SCSB tail can produce subcavitating L/D efficiency over three times greater than traditional blunt-end profiles. This superior performance in subcavitation serves to benefit high-speed propellers by "minimizing the required thrust or propulsion power (directly dependent on the hydrofoil drag)... [which] will cause less engine overload at low revolutions or during accelerations" [5].

Dr. Brizzolara has continued his exploration into the feasibility of the SCSB profile as applied to support and control surfaces of high-speed craft; however, this research is the first to apply the concept directly to a propeller.

THIS PAGE INTENTIONALLY LEFT BLANK

Chapter 2

Theory

To understand the principles by which the propeller of this report achieves effective high-speed operation, a mathematical overview of supercavitating flow is presented. We then discuss the development of supercavitating hydrofoil profiles fundamental to this propeller's design. Specifically, we outline the work of Virgil E. Johnson who performed landmark research on hydrofoils operating near the water's surface; his theory forms the backbone of our propeller's ability to achieve and sustain supercavitating flow. Finally, in order to qualify the numerical methods used to analyze the 2D hydrofoils and 3D propellers of this report, the principles behind the computational fluid dynamics (CFD) simulations are discussed with regard to unsteady multiphase flows.

2.1 Supercavitating Flow

Cavitation in a liquid is defined by the nondimensional cavitation number σ, where

$$\sigma = \frac{p_o - p_c}{q} \tag{2.1}$$

This equation presents the difference between the local absolute pressure p_o and the vapor pressure p_c, comparing that differential to the dynamic pressure q, where

$$p_o = p_{atm} + \rho g h \tag{2.2}$$

and

$$q = 0.5\rho V^2 \tag{2.3}$$

Given a depth h below the water and speed V through the water, σ defines the potential of the flow to cavitate. High values of σ indicate that the flow is unlikely to cavitate, whereas low σ effects cavitation.

Reducing σ will result in increasingly large vapor cavities extending further downstream of a submerged body in motion. When the cavitation number is sufficiently low, the cavity will extend several chord lengths while completely enclosing the suction (upper) surface of the body; meanwhile, the far-downstream cavity collapse will not impinge upon the body or its hydrodynamic characteristics. Such flow is defined as *supercavitating* [15]. Figure 2-1 shows a CFD example of this type of long vapor cavity (illustrated in red) resulting from supercavitation on a hydrofoil.

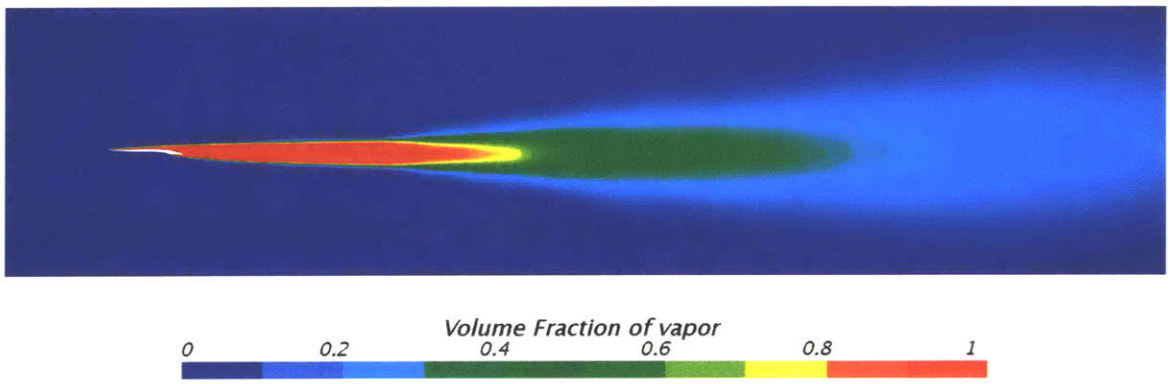

Figure 2-1: CFD example of a vapor cavity extending downstream (to the right) off a hydrofoil in full supercavitation mode (red = vapor, blue = liquid)

A low cavitation number - and thus supercavitating flow - may be achieved by either increasing the cavity pressure or the body's velocity. For the application of surface-piercing propellers and hydrofoils in general, the cavity pressure is fixed by the constant depth of operation and assumed-constant water temperature (subject to variability but beyond control). Velocity therefore becomes the primary characteristic that determines cavitation, and as such supercavitating bodies typically operate at very high speeds.

2.1.1 Superventilation

One significant caveat to the need for high speed in order to achieve supercavitation is the ability of air to substitute for the vapor cavities. When a large quantity of air is continuously supplied to the flow around a body with a separated boundary layer, the air occupies the separated region. If this quantity is sufficiently large, very long ventilation cavities will result regardless of the stream velocity. In this way, the hydrodynamic profile of supercavitation can be achieved at lower speeds than otherwise required.

Hydrofoils operating on the water surface - such as the blades of surface-piercing propellers - benefit from this phenomenon by drawing in significant amounts of air from the atmosphere. The air is entrained in the separated flow from the suction side of the foils, resulting in superventilation that covers the non-pressure regions in the same manner as vapor cavities from supercavitation. Furthermore, at small depths of submersion on the free surface, the cavity pressure is approximately equal to the ambient pressure and thus the cavity number is nearly zero. Accordingly, surface-piercing propellers are able to achieve supercavitating efficiencies at a wider range of operating speeds [15].

2.2 Johnson's Theory for Supercavitating Hydrofoils

In 1961 NASA scientist Virgil E. Johnson published his research in the concepts of supercavitation and superventilation in his seminal report *Theoretical and Experimental Investigation of Supercavitating Hydrofoils Operating Near the Free Water Surface*. Motivated by the advent of extremely high-speed craft such as the Convair F2Y Sea Dart supersonic seaplane (Figure 2-2), he sought to improve their performance as they rode on the water surface. Existing craft like the Sea Dart had been employing "hydro-skis" to skim along the surface, but Johnson believed that superior performance could be achieved through supercavitating hydrofoils.

The challenge for hydrofoils was that, as they approach the free surface, "the low-pressure side of the hydrofoil almost always becomes ventilated from the atmosphere," which "results in a severe and usually abrupt loss in lift and a reduction in the lift-drag ratio," a reduction that could exceed 75% [15]. Rather than trying to avoid the occurrence of ventilation, however, Johnson's solution was to embrace it. Building upon earlier theory developed by Marshall P. Tulin and M.P. Burkart, in his report Johnson presents theoretical approaches to develop supercavitating profiles that leverage the advantages of operating within a cavity.

Figure 2-2: High-speed craft traveling on the water's surface, such as the Convair F2Y Sea Dart supersonic seaplane, motivated Johnson to explore supercavitating hydrofoils [21].

Validating his theory with actual experimental results, the outcome was a series of equations that define the ideal shape of hydrofoil profiles that maximize lift and minimize drag while operating in supercavitation. Two series of his equations - Johnson's 3-term and 5-term profiles - formed the basis of the propeller design of this report.

2.2.1 Tulin-Burkart

The derivation of Johnson's equations stemmed from the famous work of Tulin-Burkart on *Linearized Theory for Flows About Lifting Foils at Zero Cavitation Number* [36]. This theory applied to cambered surfaces (with positive pressure on the lower side) at small angles of attack and camber. Their analysis stemmed from developed thin-airfoil theory, wherein the airfoil equations for lift, drag, and vorticity were applied to hydrofoils. The resultant Tulin-Burkart equation for hydrofoil lift/drag efficiency is:

$$\frac{C_L}{C_D} = 4\left(1 - \frac{A_2}{2A_1}\right)^2 \frac{\pi}{2C_L} \tag{2.4}$$

where the coefficients A_1, A_2 are the thin-airfoil coefficients derived from the sine-series expansion of the airfoil vorticity distribution. This distribution $\Omega(x)$ is defined by:

$$\Omega(x) = 2V\left(A_0 \cot\left(\frac{\theta}{2}\right) + \sum_{n=1}^{\infty} A_n \sin(n\theta)\right) \tag{2.5}$$

where θ is the parameter defining the distance along a hydrofoil chord such that

$$x = \frac{c}{2}(1 - \cos\theta) \tag{2.6}$$

The coefficients A_1 and A_2 serve to identify the desired input into Equation 2.4: for the maximum lift-drag ratio C_L/C_D (equivalent to L/D), the term A_2/A_1 must be minimized. In order to determine the values of these coefficients, the vorticity distribution of Equation 2.5 is considered with the assumption that only the upper surface is enveloped by the cavity. The assumption - fundamental to the concept of supercavitation - forces $\Omega(x)$ to be positive in the interval $0 \leq \theta \leq \pi$, meaning that the pressure on the hydrofoil's lower surface is positive over the entire chord. This stipulation simplifies Equation 2.5 such that:

$$\Omega(x) = 2V\sum_{n=1}^{\infty} A_n \sin(n\theta) \qquad (0 \leq \theta \leq \pi) \tag{2.7}$$

Equation 2.7 therefore describes the vorticity distribution for a supercavitating hydrofoil. Specifying that this equation be defined by only two terms and combining it with Equation 2.4, Tulin-Burkart determined that the optimum coefficient relationship is $A_2/A_1 = -1/2$. With this relationship, they were able to yield the first equation defining

an optimized hydrofoil shape:

$$\frac{y}{c} = \frac{A_1}{2}\left[\frac{x}{c} + \frac{8}{3}\left(\frac{x}{c}\right)^{\frac{3}{2}} - 4\left(\frac{x}{c}\right)^2\right] \tag{2.8}$$

where A_1 is given by:

$$A_1 = \frac{8}{5\pi}C_L \tag{2.9}$$

for zero angle of attack ($\alpha = 0$). These equations together calculate the two-dimensional pressure face coordinates x and y (in the plane aligned with the flow), corresponding to the red edge of Figure 1-5 which generates the principle lift for the hydrofoil.

Tulin-Burkhart determined that such a shape would have a lift-drag ratio 25/4 times greater than the theoretical lift-drag of a flat plate, before even considering adjustments to the angle of attack. They noted however that superior shapes are possible through consideration of greater than two terms in the vorticity distribution [36]. Johnson exploited this opportunity with the development of his 3-term and 5-term hydrofoil profiles.

2.2.2 *J3T* and *J5T* Hydrofoil Equations

Johnson picked up where Tulin-Burkart left off in order to create supercavitating hydrofoils with even greater lift-drag efficiency. Whereas Tulink-Burkart used only two terms in the vorticity distribution equation (Equation 2.7), Johnson used three and five terms to develop a series of equations that define optimal hydrofoil shapes for maximum L/D in supercavitation. The coordinates are calculated based on the objective lift coefficient C_L, angle of attack α, and chord c. Following the same derivation approach as Tulin-Burkart, he developed two new series of equations, known as Johnson's 3-term ($J3T$) and Johnson's 5-term ($J5T$) sections [15]:

$$\frac{y}{c} = \frac{A_1}{10}\left[5\left(\frac{x}{c}\right) - 20\left(\frac{x}{c}\right)^{\frac{3}{2}} + 80\left(\frac{x}{c}\right)^2 - 64\left(\frac{x}{c}\right)^{\frac{5}{2}}\right] \tag{2.10}$$

Johnson's 3-term ($J3T$) equation

$$\frac{y}{c} = \frac{A_1}{315}\left[210\left(\frac{x}{c}\right) - 2240\left(\frac{x}{c}\right)^{\frac{3}{2}} + 12600\left(\frac{x}{c}\right)^{2} - 30912\left(\frac{x}{c}\right)^{\frac{5}{2}} + 35840\left(\frac{x}{c}\right)^{3} - 15360\left(\frac{x}{c}\right)^{\frac{7}{2}}\right] \quad (2.11)$$

Johnson's 5-term (*J5T*) equation

where A_1 is calculated from C_L and α by

$$A_1 = \frac{2}{3}\left(\frac{2}{\pi}C_L - \alpha\right) \quad (2.12)$$

A_1 term for *J3T* equation

$$A_1 = \frac{3}{5}\left(\frac{2}{\pi}C_L - \alpha\right) \quad (2.13)$$

A_1 term for *J5T* equation

Figure 2-3 shows the output of the *J3T* and *J5T* equations to define respectively third- and fifth-order pressure-face profiles. Note that in this figure as throughout this paper, the convention for flow direction is left-to-right. As mentioned above, these profiles would correspond to the red edge of Figure 1-5.

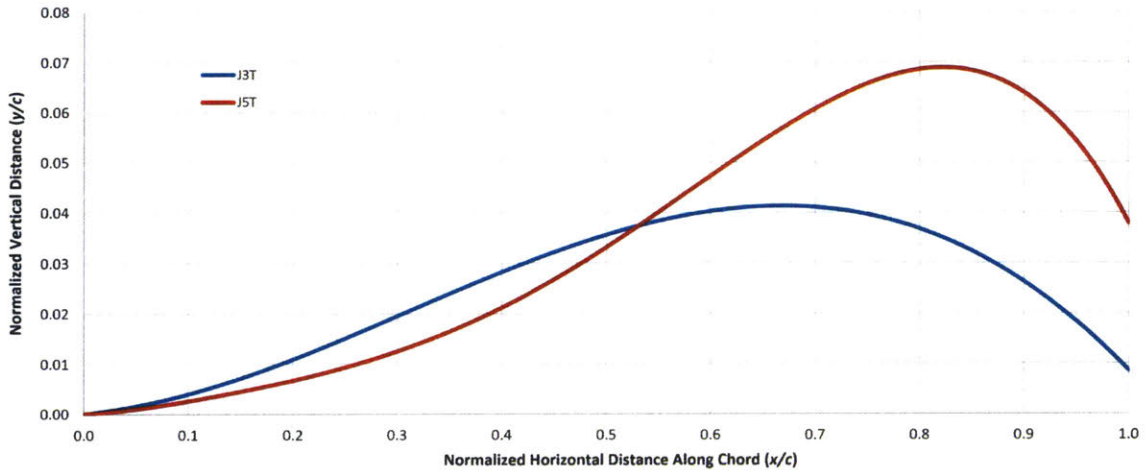

Figure 2-3: Example J3T and J5T pressure-face profiles

As illustrated in Figure 2-3, the *J5T* profile showcases not only significantly greater curvature but also greater height overall. These two facets allow it to produce superior L/D characteristics compared to the J3T form; in practice, however, these benefits may come at a cost to producibility. Regardless, both sections are significant improvements over the previous designs: according to Johnson's calculations, the *J3T* and *J5T* profiles would exhibit 9 and 11 times greater L/D, respectively, compared to flat plate theory, corresponding to 1.44 and 2 times greater than the Tulin-Burkart section. This report explored the efficacy of both profiles in supercavitating propeller blade design.

2.3 Simulation Model: RANSE Solver for Multiphase Flows

The hydrodynamics of surface-piercing, supercavitating flow demand a robust simulation architecture capable of handling complex flow. In particular, the system must be able to model three critical characteristics: cavitation, unsteady flow, and multiple fluid phases (air and water). For an accurate simulation, the system should be able to account for compressibility, condensation, evaporation, phase interaction along the free surface, and all the associated kinematics. The precise modeling of such aggregate phenomena is a significant challenge even with advanced CFD software.

For an engineering analysis, however, the principle hydrodynamic effects can be sufficiently captured through a Reynolds-Averaged Navier-Stokes (RANSE) solver using multi-fluids continuum theory. In this construct, several simplifications are applied to the flow. First, the fluids are considered to be incompressible, thereby neglecting the acoustic scale of the phenomena. The air is further simplified by assuming it isothermal and immiscible. For the phase-change of the water as a result of cavitation, the Volume of Fluids (VoF) approach provides the means to capture the fluid interface.

The foundation of the RANSE solver are the classical Navier-Stokes equations for the fluid mixture:

$$\nabla \cdot V = \frac{\dot{m}}{\rho_{liquid}} \tag{2.14}$$

$$\frac{D}{Dt}(\rho_{mix} V) - \nabla \cdot (\mu_{mix} \nabla V) - (\nabla V \cdot \nabla \mu_{mix}) = \nabla \cdot T_{R_e} - \nabla p \tag{2.15}$$

$$\frac{\delta \alpha_{liquid}}{\delta t} + \nabla \cdot (\alpha_{liquid} V) = \frac{1}{\rho_{liquid}} - \frac{1}{\rho_{vapor}} \dot{m} \tag{2.16}$$

$$\frac{\delta \alpha_{air}}{\delta t} + \nabla \cdot (\alpha_{air} V) = 0 \tag{2.17}$$

where α_{liquid}, α_{vapor}, and α_{air} represent the phase concentrations, adhering to the conservation equation $\alpha_{liquid} + \alpha_{vapor} + \alpha_{air} = 1$. The classical Navier-Stokes equations (2.15, 2.16, 2.17) together with a modified version of the continuity equation (2.14) resolve the phase change from liquid to vapor as a result of the cavitation and unsteady flow. Furthermore, for a single cell within the simulation mesh, these four equations solve for the quantity of each phase within that cell [7].

The important rate of phase change is determined via the Schnerr-Sauer model for unsteady cavitating flow. The basis of this model is the Rayleigh-Plesset equation describing the dynamic equilibrium of a vapor bubble (of radius R_B) to an external pressure p and surface tension σ:

$$R_B \frac{d^2 R_B}{dt^2} + \frac{3}{2}\frac{d^2 R_B}{dt^2} + \frac{2\sigma}{R_B} = \frac{p_{vapor} - p}{p_{liquid}} \tag{2.18}$$

The Shnerr-Sauer model is then applied ot the RANSE solver with the aforementioned simplifications to model the vapor phase dynamics through the following differential equation for mass flow:

$$\dot{m} = -3\rho_{vapor}\left[n_0 \frac{4}{3}\pi\left(\alpha^2 - \alpha^3\left(1 - \frac{\rho_{vapor}}{\rho_{liquid}}\right)\right)\right]^{\frac{1}{3}} \cdot \operatorname{sign}(p_{vapor} - p) \cdot \left(\frac{2}{3}\frac{|p_{vapor} - p|}{\rho_{liquid}}\right)^{\frac{1}{2}} \tag{2.19}$$

where n_0 is the initial mean diameter of a bubble inside the fluid. Through this equation, the unsteady multiphase flow involving water, vapor, and air is solved in a RANSE simulator such as *STAR-CCM+* [7] [30].

Chapter 3

Design Baseline

Designing a propeller from scratch requires significant complex analyses to determine every aspect of the geometry (from radial length to rake angle) as well as the operational profile (from rotational velocity to the host craft's operating speed). The process consists of "discrete analysis modules in which momentum theory, blade planform corrections, and section design are sequentially considered in the course of an iterative convergence toward some specified radial thrust distribution" [31]. While this would certainly result in an entirely new design, such a process unfortunately would exceed the time and resource limitations of this study.

Therefore, in order to enable the design focus to remain exclusively on the blade hydrofoil geometry, an existing surface-piercing, supercavitating propeller was selected as a baseline on which to base all other parameters. This not only reduced the number of initial unknowns for the design, but it ensured that the selected parameters were suitable to such a design since they stem from an existing, proven propeller. Specifically, the parameters adopted from the baseline design were:

- Number of blades
- Propeller diameter
- Pitch
- Rake
- Skew
- Chord lengths along radius
- Hub diameter and shape
- Propeller rotational speed
- Vessel design speed

From this baseline, the blade sections were amended using Johnson's theoretically optimal foils (Section 2.2) in an effort to improve supercavitating performance. Additionally, the unique trailing edge SCSB "tail" was added to enhance performance in the subcavitating regime.

In addition to providing certain parameters on which to base the design, the baseline propeller provided the benchmark for comparison in all analyses. 2D profile sections were designed to meet or exceed the performance of their corresponding baseline sections, and the final 3D analyses determined the relative performance of the complete design.

3.1 Baseline Propeller Characterization

The selected baseline propeller came from Mercury Marine, an American company with extensive experience in high-speed propeller engineering. Specifically, this design selected a Mercury racing propellers (Figures 3-1 and 3-2) designed to achieve speeds in excess of 100 knots. It features a traditional supercavitating foil profile, with a sharp leading edge and blunt trailing edge. Mercury has successfully implemented this propeller on high-performance racing craft such as the Fountain *Lighting* (Figure 1-4).

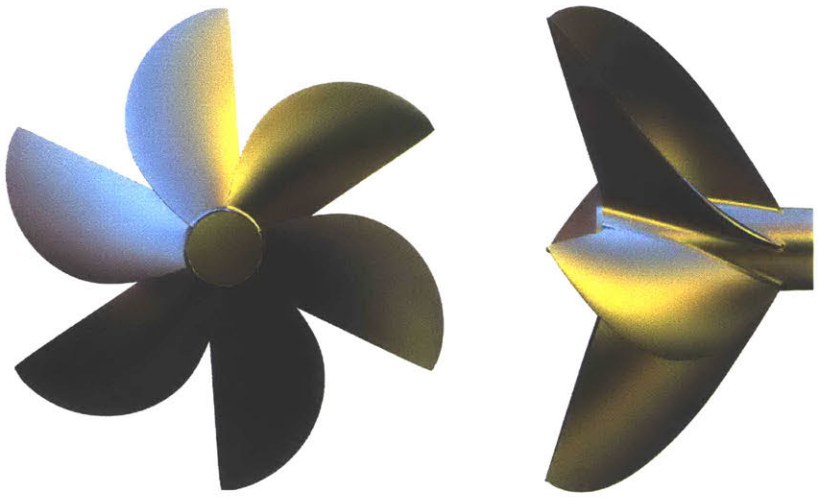

Figure 3-1: Baseline Mercury racing propeller (front and side views)

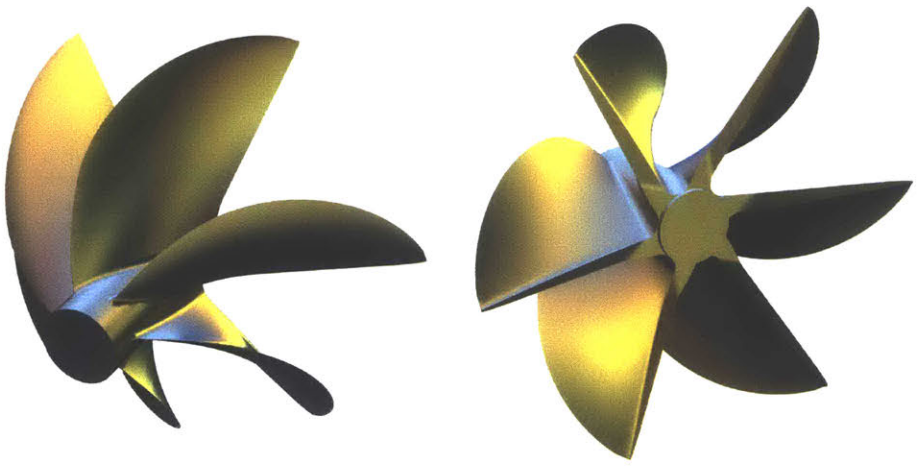

Figure 3-2: Baseline Mercury racing propeller (isometric views)

Table 3.1: Baseline propeller geometry and operating parameters [32]

Parameter	*Symbol*	*Value*	*Units*
Number of Blades	N	6	-
Diameter	D	17	in
		0.4318	m
Pitch	P	35	in
		0.8890	m
Rake	θ_i	15	degrees
Skew	θ_s	0	degrees
Leading Edge Blade Thickness	t_{LE}	0.015	in
		0.0004	m
Hub Diameter (Forward)	$D_{hub-fwd}$	35	in
		0.8890	m
Hub Diameter (Aft)	$D_{hub-aft}$	35	in
		0.8890	m
Propeller Rotational Speed	n	4570	rpm
		76.17	rps
Vessel Design Speed	V	130	mph
		113	knots
		58.12	m/s
Propeller Submergence (below shaft centerline)	h_{sub}	2.4	in
		0.061	m

The dimensions and operating characteristics constant to the overall propeller are listed in Table 3.1. The blade profile dimensions that vary along the radius (referenced at fractions of the total radius, r/R) are presented in Table 3.2. Units have been converted from originating document units to those used in subsequent calculations where applicable. These parameters were applied to the new propeller for both design and analysis.

In order to facilitate the new design based on the Mercury baseline, certain additional parameters needed to be determined for the characterization of the flow. These parameters were the pitch angle φ, inflow angle β, angle of attack α, relative velocity V_{rel}, which were calculated as follows:

$$\varphi = arctan\left(\frac{P}{2\pi r}\right) \tag{3.1}$$

$$\beta = arctan\left(\frac{V}{2\pi nr}\right) \tag{3.2}$$

$$\alpha = \varphi - \beta \tag{3.3}$$

$$V_{rel} = \sqrt{V^2 + (2\pi nr)^2} \tag{3.4}$$

$$R_e = \frac{V_{rel}c}{\nu} \tag{3.5}$$

where the kinematic viscosity $\nu = 8.9266 \times 10^{-07}$ m^2/s for freshwater at 25°C. Additionally, the inflow velocity V_{in} and reference pressure p_{ref} needed to be calculated for each section in order to facilitate the subsequent flow simulations:

$$V_{in} = \frac{R_e\nu}{c_{ref}} \tag{3.6}$$

$$p_{ref} = \frac{1}{2}p_v\sigma_o\rho V_{in}^2 \tag{3.7}$$

where the reference chord length $c_{ref} = 1$ m, the vapor pressure of freshwater at 25°C $p_v = 3300$ Pa, and the water density $\rho = 997.0476$ kg/m^3. The calculated values are listed in Table 3.3 and are used for the ensuing 2D simulations and subsequent development of original blade profiles.

Note: additional radial blade profiles were used in the baseline propeller characterization than are listed in Tables 3.2 and 3.3; however, these were omitted in order to protect company proprietary information.

Table 3.2: Baseline propeller blade profile dimensions along the radius [32]

Parameter	*Symbol*	*Values*				*Units*
Normalized Local Radius	r/R	0.30	0.50	0.70	0.90	-
Local Radius	r	2.55	4.25	5.95	7.65	in
		0.065	0.108	0.151	0.194	m
Local Chord	c	5.70	5.70	5.17	3.20	in
		0.145	0.145	0.131	0.081	m
Blade Thickness (Trailing Edge)	t_{TE}	0.580	0.405	0.255	0.120	in
		14.7	10.3	6.49	3.05	mm
Pitch	P	34.8	34.4	34.0	33.6	in
		0.885	0.875	0.865	0.855	m

Table 3.3: Calculated operating parameters for the baseline propeller blade profiles

Parameter	*Symbol*	*Values*				*Units*
Normalized Local Radius	r/R	0.30	0.50	0.70	0.90	-
Pitch Angle	ϕ	65.30	52.21	42.32	34.99	deg
Inflow Angle	β	61.93	48.36	38.78	32.00	deg
Angle of Attack	α	3.378	3.847	3.536	2.983	deg
Relative Velocity	V_{rel}	65.86	77.76	92.78	109.7	m/s
Reynold's Number ($\times 10^6$)	R_e	8.375	9.887	10.70	7.816	-
Inflow Velocity	V_{in}	7.476	8.826	9.552	6.977	m/s
Reference Pressure	p_{ref}	4693	5242	5574	4514	Pa

3.2 Baseline 2D CFD Results

The final parameters required from the baseline profiles necessitated computational fluid dynamics (CFD). Four representative sections were used - $r/R = 0.3, 0.5, 0.7, 0.9$ - to quantify the blade characteristics. The simulations were conducted using Siemen's software *STAR-CCM+* to run two-dimensional flow analyses on each section [33]. The full profile geometries were provided by Mercury, and each section was normalized to the reference chord length (c_{ref}) of one meter. The requisite parameters for the simulations were as developed in the preceding section.

The objective of these simulations was to assess the lift coefficient (C_L) and drag coefficient (C_D) of each profile, which in turn determined the overall measure of efficiency, lift-over-drag ($L/D = \frac{C_L}{C_D}$). These results are tabulated in Table 3.4. The full plot of results over time are provided in Figure 3-3 as an example to demonstrate that simulations were run sufficiently long in order to achieve stable steady-state solutions. All 2D CFD simulations for both propellers were run for a similar duration.

An additional - and equally important - objective was to capture the supercavitating behavior of the hydrofoils as they operate at the design speed V_{in}. The supercavitation effect is visualized in the *Volume of Fluid* images of Figure 3-4, where blue indicates the full liquid state and red indicates full vapor.

Table 3.4: Results of 2D CFD simulations on Mercury hydrofoil sections

Parameter	*Symbol*	*Values*				*Units*
Normalized Local Radius	r/R	0.30	0.50	0.70	0.90	-
Lift Coefficient	C_L	0.127	0.293	0.300	0.304	-
Drag Coefficient	C_D	0.0219	0.0292	0.0289	0.0289	-
Lift-over-Drag	L/D	5.82	10.02	10.39	10.51	-

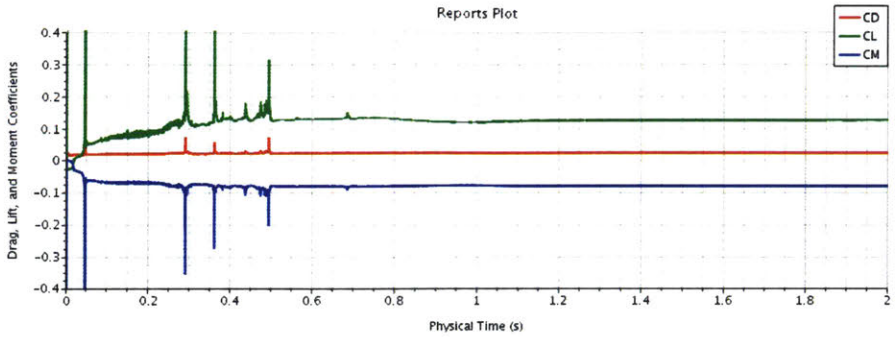

(a) $r/R = 0.3$

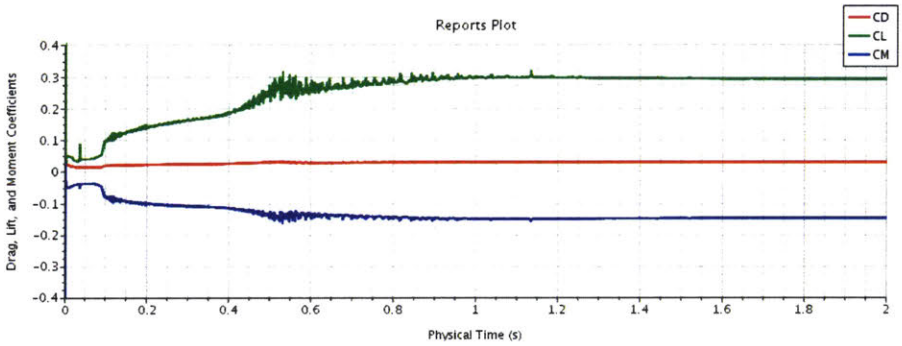

(b) $r/R = 0.5$

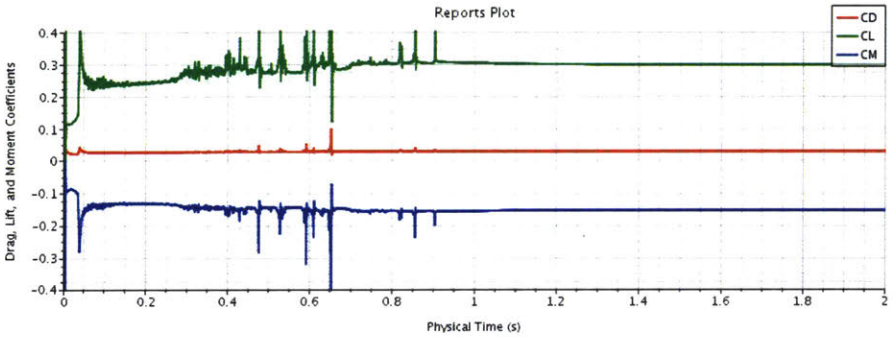

(c) $r/R = 0.7$

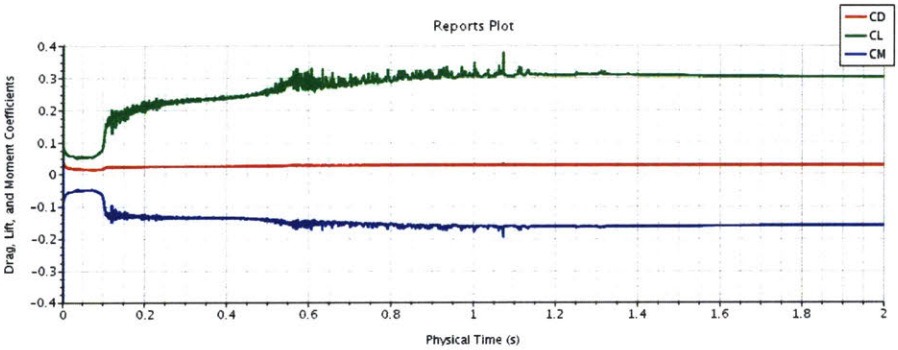

(d) $r/R = 0.9$

Figure 3-3: Lift, drag, & moment results of 2D CFD on Mercury hydrofoils

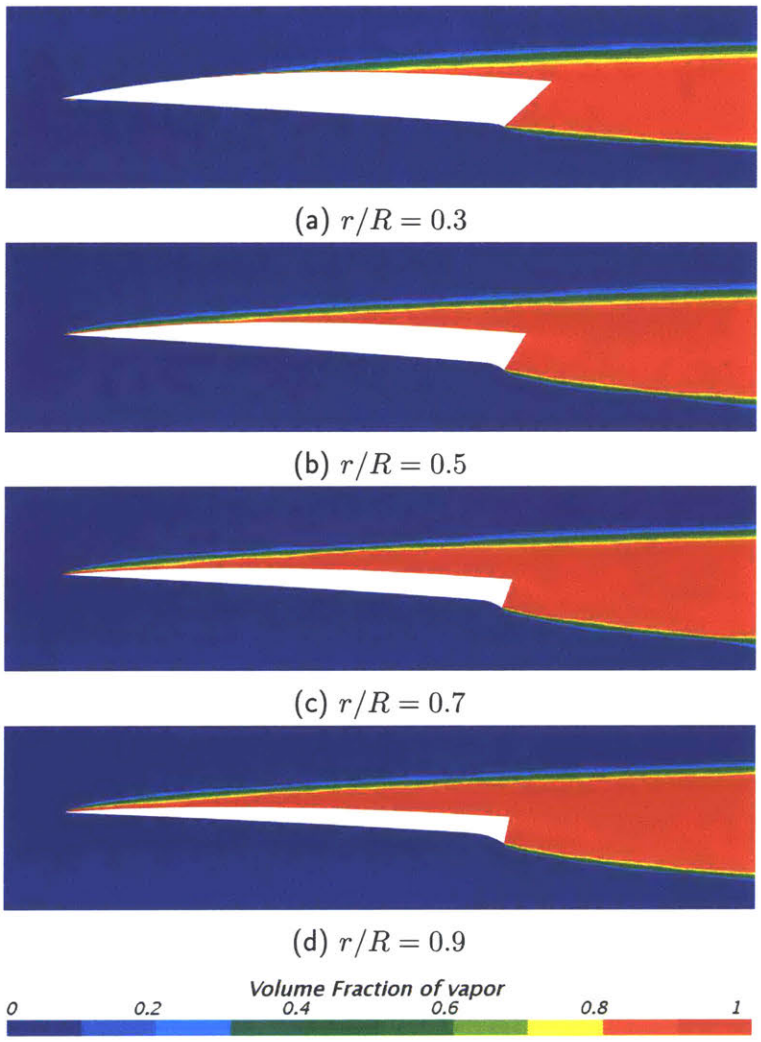

Figure 3-4: 2D CFD results for baseline Mercury hydrofoils showing volume of fluid (red = vapor, blue = liquid)

THIS PAGE INTENTIONALLY LEFT BLANK

Chapter 4

New Propeller Design

Having sufficiently quantified the baseline propeller, the new design could proceed. The process of developing the new hydrofoils followed the "hybrid CFD-theoretical design method" formulated by Brizzolara and Federici [6]. This method employs three basic steps to develop a supercavitating profile:

1. Draw the pressure-face lines from Johnson's theory;
2. Use 2D CFD simulations to inform the shape of the non-pressure (back and trailing edge) surfaces, ensuring full cavity envelopment through trial-and-error of the simulations;
3. Ensure sufficient strength (modulus of inertia) for the entire hydrofoil section.

Following this process, the design began with the pressure face (corresponding to the red face of Figure 1-5) - the necessary starting point as its geometry has the greatest impact on overall hydrofoil performance. The back and tail were then drafted, making iterative adjustments based on CFD results and strength analysis. Refinements to the entire profile continued until all design objectives were met.

To characterize the full propeller blade, the same four radial sections as on the baseline were developed and analyzed: $r/R = 0.3, 0.5, 0.7, 0.9$. Additional sections were subsequently created as extensions of the core four profiles in order to refine the surface curvature close to the hub and tip. By employing a series of equations to translate the 2D hydrofoils into 3D space, the full propeller geometry was established.

4.1 Design Objectives

The overarching objective was to meet or exceed the Mercury performance (based on the CFD analysis of Table 4.1) while maintaining the same geometric and operational constraints listed in Tables 3.1 and 3.3. An additional requirement was for the new foils to operate in a supercavitating mode such that the vapor cavities resembled those of their respective baseline sections. Specifically, the design goals for each hydrofoil section were as follows:

- **Lift-to-drag ratio**: meet or exceed L/D for the respective baseline section
- **Lift coefficient**: achieve $C_L \geq 0.30$
- **Supercavitation**: ensure vapor cavities fully enclose non-pressure surfaces, with cavities of similar size as the respective baseline section
- **Subcavitating performance**: achieve $C_L \geq 0.6$ via the tail design
- **Producibility**: limit complex curvature as much as practicable while meeting hydrodynamic requirements to support manufacturing producibility considerations
- **Strength**: Improve the strength of each section, as measured by section modulus S, by 30%

With these goals in mind, the design followed the Brizzolara-Federici method to iteratively converge upon the hydrofoil shapes that optimally satisfied the above conditions. Once these were achieved and the complete 3D propeller geometry created, the new propeller was compared to the baseline in full 3D CFD analyses, where the desired outcome was increased thrust at the same (or lower) torque on each blade. Although the thrust and torque comparisons were the ultimate assessment of the propeller's relative efficacy (presented in Chapter 5), these analyses were an end result rather than a design objective that informed the hydrofoil geometry development. The focus of the design itself therefore rested on the above list of objectives.

4.2 Hydrofoil Profile Development

The design of the blade profiles began with the theoretical optimal pressure face profiles developed by Johnson (Section 2.2). The first attempt used his 3-term equation (Equation 2.10); since its curvature is simpler than that of the 5-term, it was a more desirable form from a manufacturing perspective. Considering this producibility aspect, if satisfactory L/D could have been achieved using the *J3T* form then it would be the preferred candidate for the blade design.

As a starting point, the section at $r/R = 0.7$ was developed first - its high efficiency ($L/D = 10.39$) and near-full chord length ($c = 0.131$ m) relative to the other sections made it a preferred candidate for optimization. Once satisfactory results were achieved, the ensuing sections at $r/R = 0.3, 0.5, 0.9$ were built upon the results of 0.7.

4.2.1 *J3T* Profile

Combining the baseline propeller characteristics and Johnson's equations, the resultant pressure face was as shown in Figure 4-1. The remaining unknown regarding the face was the angle at which it should be inclined relative to the flow for maximum lift and minimum drag. Although this angle of attack α was determined for the Mercury sections, the angles were not actually comparable between the Johnson and Mercury blades due to the relative inclination of the face camber. Whereas the Mercury profiles had flat faces defined to be perfectly parallel with the x-axis, the Johnson profiles each had an inherent declination to their camber; that is, their aftermost point (at $r/R = 1.0$) was higher than their forwardmost point (at $r/R = 0.0$). The Mercury angles of attack were used as a starting point, however multiple CFD simulations were required to establish the most optimal angle of attack to maximize L/D.

Although the first objective was to solely assess the performance of the face profile, the other sides of the profiles had to be developed in order to facilitate the simulations. Representative back - and later tail - curves were added to the face curve to develop a closed profile; however, significant attention was not paid to their design until the pressure face was confirmed.

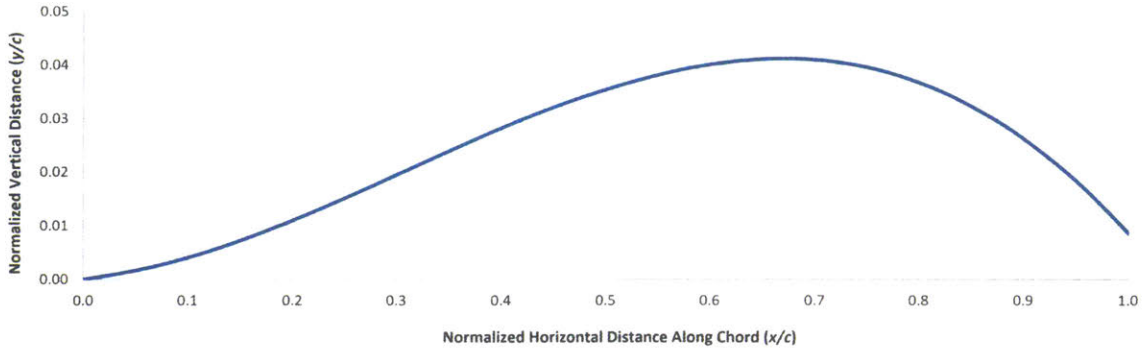

Figure 4-1: J3T profile at $r/R = 0.7$

Examples of early 2D CFD simulations on the *J3T* sections are shown in Figure 4-2. The sequence of images illustrates the initial development of the profiles: Figure 4-2a shows the unadulterated *J3T* profile at the baseline Mercury angle of attack, with a nominal back profile; the angle of attack was increased in Figure 4-2b to increase the lift coefficient and also ensure that the vapor cavity covered the entire

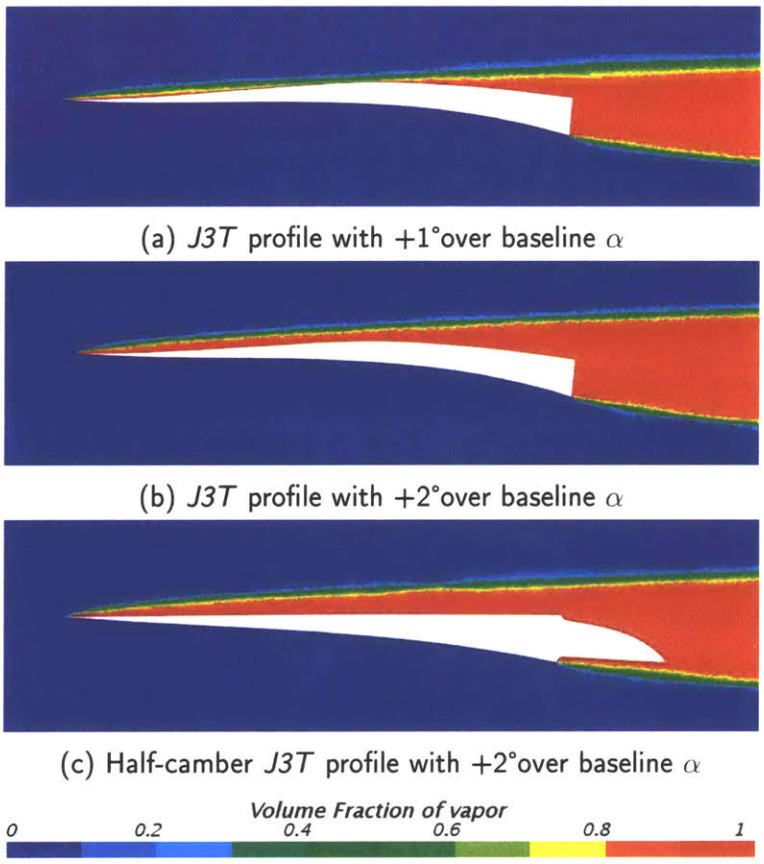

(a) *J3T* profile with +1°over baseline α

(b) *J3T* profile with +2°over baseline α

(c) Half-camber *J3T* profile with +2°over baseline α

Figure 4-2: Profile development of *J3T* face profile to determine optimal face camber and angle of attack (red = vapor, blue = liquid)

back; a tail was added in Figure 4-2c, ensuring that it remained within the cavity. Also in the final figure, the camber of the face profile was halved (i.e. the pressure face curve was scaled by $1/2$ in the vertical y direction) in order to limit the curvature for real-world producibility.

After multiple iterations, the CFD analysis of the *J3T* profile demonstrated that the *J3T* was unable to outperform the Mercury section. Although the full-cambered profile performed well (achieving $C_L = 0.306$ and $L/D = 13.18$ with $\alpha = +2$ over baseline), once the camber was halved both C_L and L/D remained well below their baseline counterpart despite various adjustments to α. The *J3T* was therefore abandoned in favor of the expected-superior *J5T*.

4.2.2 *J5T* Profile

The *J5T* profile was developed in the same manner as the *J3T*, this time using Johnson's 5-term equation (Equation 2.11) to develop the section at $r/R = 0.7$. The resultant face profile is shown in Figure 4-3, along with the three other primary sections used in subsequent development. Notably, the 0.5, 0.7, and 0.9 profiles have significant and similar curvature, whereas the 0.3 profile curvature is shallow. This correlates with the respective baseline 0.3 section and is representative of this section's relatively low contribution to lift as compared to the others.

CFD analysis of the 0.7 section immediately revealed the superior performance of

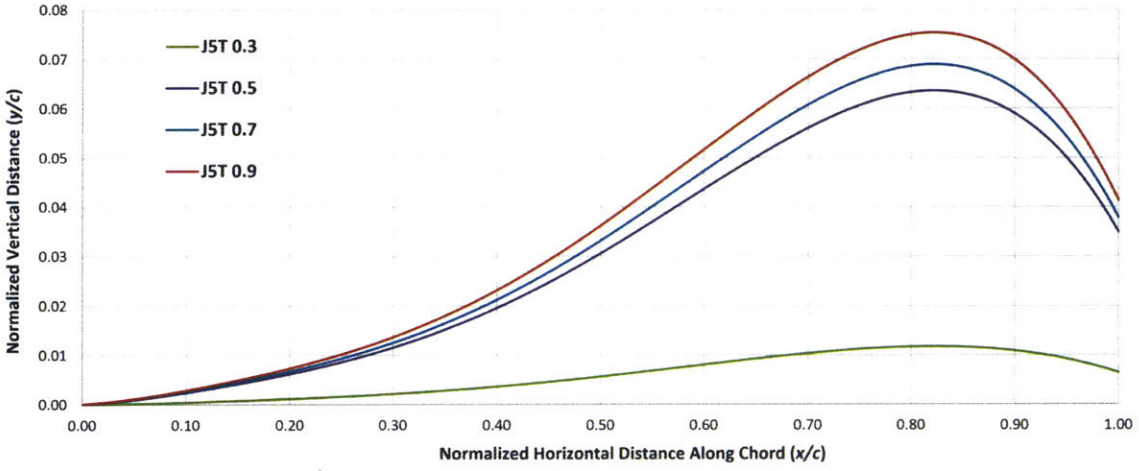

Figure 4-3: J5T profiles at $r/R = 0.3, 0.5, 0.7, 0.9$

Table 4.1: 2D CFD results for final 3/4-camber *J5T* hydrofoil sections

Parameter	*Symbol*	*Values*				*Units*
Normalized Local Radius	r/R	0.30	0.50	0.70	0.90	-
Angle of Attack	α	5.84	6.31	6.00	5.45	deg
Lift Coefficient	C_L	0.177	0.298	0.299	0.286	-
Drag Coefficient	C_D	0.0244	0.0303	0.0286	0.0246	-
Lift-over-Drag	L/D	7.25	9.84	10.45	11.61	-

the *J5T* as compared to the *J3T*, with the half-camber *J5T* exhibiting both C_L and L/D values higher than the half-camber baseline. In an effort to elicit even higher lift, the face camber was increased to an intermediate 3/4-camber profile. Although this would negatively affect producibility, a qualitative assessment determined that the improved performance justified the heightened curvature.

Through multiple iterations, satisfactory results were achieved in accordance with the design objectives. Running the CFD simulation in a "fully-wet" subcavitating condition (setting $\sigma = 2.0$) confirmed the desired lift, achieving $C_L = 0.684$. Once the 0.7 section was optimized, the remaining three sections were constructed through the combination their face profiles (from Figure 4-3, scaled to 3/4-camber) and the 0.7 profile parametrically adjusted according to their respective baseline sections. For example, having determined a 6°incline to be the optimal angle of attack for $r/R-0.7$, the other sections were inclined to the same relative degrees as the baseline sections (per Table 3.3).

The results of the final *J5T* designs are listed in Table 4.1. The three primary sections at $r/R = 0.5, 0.7, 0.9$ all achieved a lift coefficient very near $C_L = 0.3$, within 5% (the section at $r/R = 0.3$ did not produce significant lift on either the baseline or the *J5T*; nevertheless, the *J5T* profile exceeded the baseline in C_L). Furthermore, the 0.3, 0.7 and 0.9 sections attained lift-over-drag ratios superior to their respective baselines, while the 0.5 section fell less than 2% below its respective baseline.

While iterating to achieve satisfactory C_L and L/D, volume of fluid representations from the CFD simulations were inspected to assess the supercavitation performance (Figure 4-4). The final profile designs showed full vapor cavities across the back and tail of the $r/R = 0.5, 0.7, 0.9$ sections, with the cavity height commensurate with their respective baselines. Notably the 0.3 section does not achieve full supercavitation across its back, however this performance was similar on the Mercury 0.3 section.

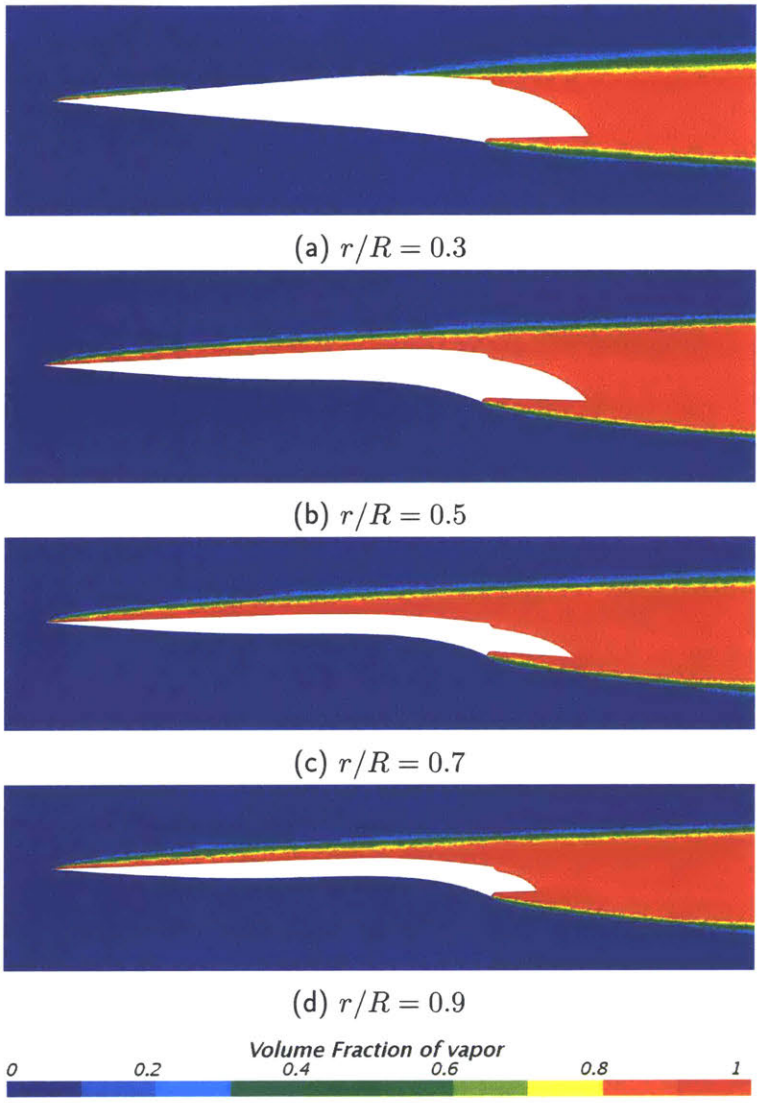

Figure 4-4: 2D CFD results for new *J5T* hydrofoils showing volume of fluid (red = vapor, blue = liquid)

With adequate lift coefficients, lift-over-drag ratios, and supercavitation vapor cavities, these $^3/_4$-camber *J5T* sections were selected for development into the full propeller blade.

4.3 Strength Verification

An additional consideration unrelated to hydrodynamic performance was the structural integrity of each section. The design had to ensure that each section - and thus the entire propeller blade - was strong enough to withstand the substantial hydrodynamic forces of the rapidly rotating propeller. Since the Mercury sections were known to have sufficient strength given that they operate on an existing propeller, their values were again used as the baseline for the new designs.

The key measurement employed to define the strength of each section was the section modulus S, which for the hydrofoil is defined as:

$$S = \frac{I_2}{t_{max}/2} \tag{4.1}$$

where t_{max} was the maximum profile thickness and I_2 was the "area principal moment of inertia about the centroid and principal axes" as measured by the computer-aided design (CAD) software *Rhino* [27]. Given that the profiles were two-dimensional, each had two corresponding area principal moments of inertia; the smallest of these was used for analysis as it corresponded to the axis of least strength.

As evidenced in Table 4.2, the final *J5T* section designs successfully achieved the desired +30% increase in section modulus, within +/- 3%. The profiles were therefore assessed to have sufficient strength to proceed with full blade development.

Table 4.2: Strength comparison between Mercury and *J5T* hydrofoil sections

	Parameter	*Symbol*	*Values*				*Units*
Normalized Local Radius		r/R	0.30	0.50	0.70	0.90	-
Mercury	Area Principal Moment of Inertia ($\times 10^{-5}$)	I_2	5.539	2.004	0.741	0.436	m^4
	Maximum Thickness	t_{max}	0.105	0.075	0.053	0.043	m
	Section Modulus ($\times 10^{-4}$)	S	10.55	5.345	2.797	2.026	m^3
J5T	Area Principal Moment of Inertia ($\times 10^{-5}$)	I_2	10.54	3.756	1.308	0.941	m^4
	Maximum Thickness	t_{max}	0.154	0.110	0.073	0.070	m
	Section Modulus ($\times 10^{-4}$)	S	13.69	6.829	3.584	2.688	m^3
Percent increase in S from Mercury to *J5T*			29.8	27.8	28.1	32.7	%

4.4 3D Blade Generation

With the four radial sections at $r/R = 0.3, 0.5, 0.7, 0.9$ fully defined and analyzed for performance, additional sections were developed in order to define the full propeller blade. These sections were taken at $r/R = 0.15, 0.20, 0.97, 1.00$ in order to ensure that the blade was well-defined near the hub and tip. CFD was not conducted on these sections, however; instead, their profiles were geometrically extrapolated from the already-defined four sections and the relative change in chord lengths per Table 3.2. All sections were reduced from the reference chord length of one meter to their actual chord lengths corresponding to the baseline blade.

In order to convert the 2D sections into an accurate 3D geometry, the two-dimensional x, y points of each profile had to be translated to three-dimensional polar coordinates x_p, y_p, z_p. To accomplish this, the following series of equations were used [9]:

$$\begin{aligned} x_p &= -\left[i_G + r\theta_s \tan(\varphi)\right] + x\sin(\varphi) + y\cos(\varphi) \\ y_p &= r\sin\left[\theta_s - \frac{x\cos(\varphi) - y\sin(\varphi)}{r}\right] \\ z_p &= r\cos\left[\theta_s - \frac{x\cos(\varphi) - y\sin(\varphi)}{r}\right] \end{aligned} \tag{4.2}$$

where θ_s is the skew, φ is the pitch angle, x, y are the two-dimensional profile coordinates, the generator line rake $i_G = r\tan(\theta_i)$ (with θ_i as the rake angle). The angle values were populated from Tables 3.1 and 3.3, converted to radians for use in the equations as shown. Note that certain symbology has been amended from the original text for consistency in this report. Additionally, the original equations adjust the x coordinates to account for a mid-chord ($0.5c$) reference point; as the *J5T* sections are defined about the aftermost point of the face profile, this term is not required and therefore removed from the equations.

To define each profile by x, y points, each 2D CAD curve was subdivided into 10,000 points in *Rhino*. This high number of points ensured that the complex curvature was fully captured; additionally, special attention was paid to capturing corner points. The data set was then run through a *Matlab* script (provided in Appendix A) to facilitate Equation 4.2. Once imported back into *Rhino*, the result of this conversion is shown in Figure 4-5.

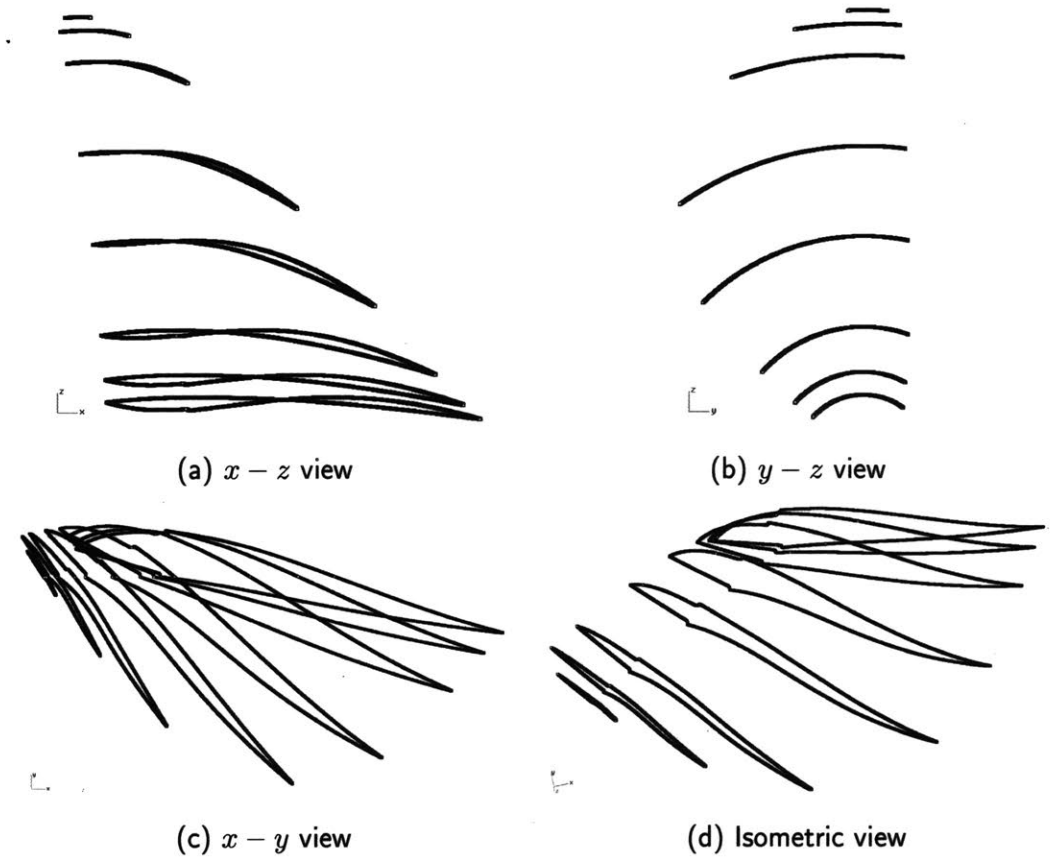

(a) $x - z$ view (b) $y - z$ view

(c) $x - y$ view (d) Isometric view

Figure 4-5: *J5T* 3D sectional curvature

With each curve still defined by 10,000 points, the actual curves had to be recreated. These were formed by interpolating the points of each side separately: the face, the back, and both top and bottom of the tail. The leading edge curvature was also captured separately due to its distinctly small radius. Once interpolated, the curves were refined using the "FitCrv" command within *Rhino* in order to smooth out any local irregularities. All curves were fit to a 3^{rd}-order curve with the exception of the face which was fit to a 5^{th}-order curve since its original 2D curve was formed using a $>3^{rd}$-order equation in Equation 2.11.

The individual curves were then used to create the 3D blade surfaces. Three different *Rhino* methods of surface generation were attempted: loft, network, and 2-rail sweep. Ultimately the loft method was shown to produce the smoothest surfaces. After lofting each of the separate curves on each section, the resultant five surfaces were joined to form the completed blade. After defining the hub (per Table 3.1) and repeating the blade around its circumference for a total of six blades, the full propeller design was complete (Figures 4-6 and 4-7).

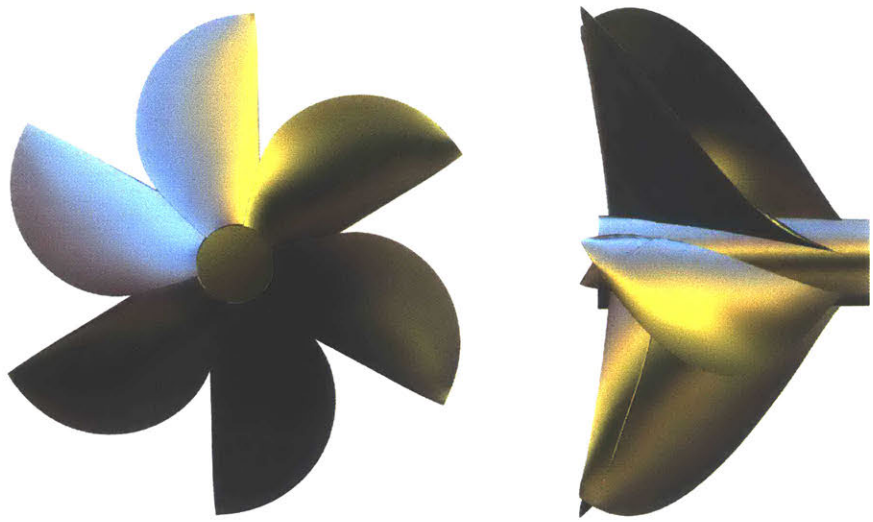

Figure 4-6: *J5T* Propeller Final Design (front and side views)

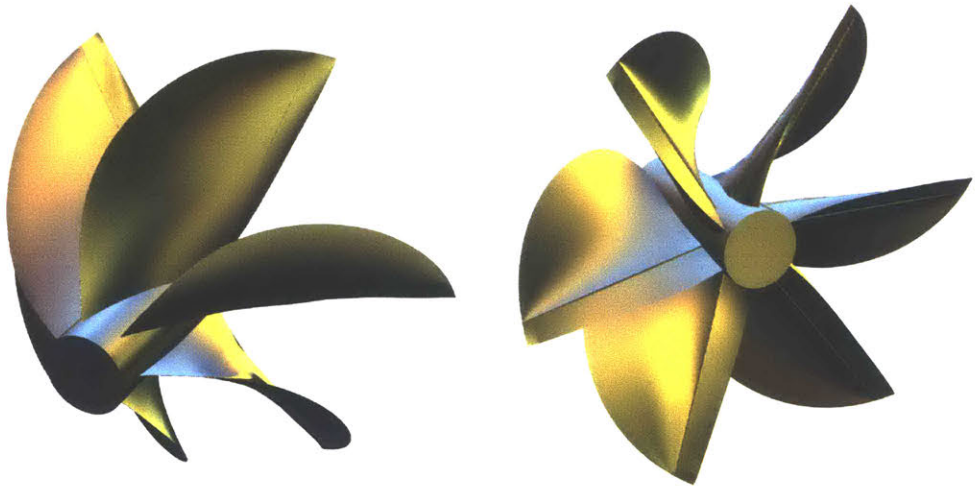

Figure 4-7: *J5T* Propeller Final Design (isometric views)

THIS PAGE INTENTIONALLY LEFT BLANK

Chapter 5

Full Propeller Analysis

Having fully characterized baseline Mercury propeller and constructed the new *J5T* model, the two propellers were prepared for a full comparative analysis using 3D CFD. The program employed for these simulations was again *STAR-CCM+*, having been proven reliable for 3D multiphase simulations in other experiments [6]. Multiple iterations of simulations were attempted before converging on a final setup that provided results sufficiently stable and accurate for the analysis.

The objective of the analysis was to determine the thrust T generated by each propeller, as well as the torque Q on the blades when producing the thrust. In order to explore their performance across a range of speeds, each propeller was subject to three separate simulations based on the advance ratio J, in accordance with standard propeller analyses wherein T and Q are plotted against J. The advance ratio is defined as:

$$J = \frac{V_a}{nd} \tag{5.1}$$

where, as before, V_a is the advance speed, n is the propeller rotational speed, and d is the propeller diameter. With the diameter fixed, the two variables available were V_a and n. The decision was made to keep n fixed based on previous analytical procedures; therefore, the advance speed was adjusted to achieve different values of J.

The advance ratios were selected based on multiplicative factors of the baseline J - that is, the advance ratio from the baseline operating characteristics ()as detailed

Table 5.1: Advance Ratios and Speeds for 3D CFD Simulations

Parameter	*Symbol*	*Values*				*Units*
J Multiplication Factor		1	1.25	0.667	0.5	-
Advance Ratio	J	1.767	2.209	1.178	0.884	-
Advance Speed	V_a	58.115	72.644	38.743	29.058	m/s

in Section 3.1) was multiplied by different factors chosen to achieve a representative spectrum of operation. The advance ratios and associated speeds are listed in Table 5.1. Note that although $1.25J$ is listed in the table and was attempted in simulations, its results were unreasonable (i.e. showing negative thrust) and therefore were not included in this report. This is however consistent with the baseline J corresponding to the maximum performance of the propeller. Also note that where J is referenced with a multiplication factor in this report (i.e. $1.25J$), the reference is to the baseline advance ratio.

With three advance ratios selected and two propellers, a total of six simulations were conducted and analyzed for performance in thrust and torque. The setup of the simulations is first presented in Section 5.1, followed by a discussion of the general flow observations. The final results for both propellers are presented in detail in Sections 5.3 and **??**.

5.1 Simulation Setup

Using *STAR-CCM+*, the propeller CAD models were imported using the finest resolution. Simulation files were then constructed based on the latest methods, following the *overset mesh* process. Multiphase physics were invoked to model the free surface interaction of air and water surrounding the rapidly rotating propeller.

5.1.1 Overset Mesh and Regions

The keystone of the simulation was the *overset mesh* model. As the contemporary method for performing CFD motion analysis, overset meshes allow a region in motion (known as the *overset region*) to interface with the background region with minimal integration requirements. To understand how this algorithm works and why it is preferred, the *Star-CCM+* User Guide provides a description:

> In an overset mesh, cells are grouped into active, inactive, or acceptor cells. Within active cells, discretized governing equations are solved. Within inactive cells, no equation is solved, however, these cells can become active if the overset region is moving. Acceptor cells separate active and inactive cells in the background region and are attached to the overset boundary in the overset region. Acceptor cells are used to couple solutions on the two overlapping grids. Variable values at donor cells of one mesh express variable values at acceptor cells in the other mesh, through interpolation. The donor cells are the active cells from the other mesh that are nearest the acceptor cell. The available interpolation options are described in the coupling regions section.
>
> The solution is computed for all active cells in all regions simultaneously, that is, the meshes are implicitly coupled. When a reference is made to the variable value in an acceptor cell of one mesh within the discretized equations, a blend of variable values at donor cells from the other mesh is used. This value is reflected directly in the coefficient matrix of the algebraic equation system. This tight coupling of the overset and background regions allows for a solution that is within an arbitrary low level of iteration errors [33].

In our simulation, the propeller was the overset region, contained within a cylinder rotating at the propeller speed n. The cylinder was sized to allow the requisite 5-cell overlap between overset and background without impeding on the propeller surface, making it 0.515 m long with a diameter of 0.622 m. The background region was formed as a box sufficiently long so as to allow the flow to adequately dissipate. Using previous propeller simulations as a guideline, the box was sized at 7.20 m long by 2.59 m high by 1.38 m wide. The background box and overset cylinder are pictured in Figure 5-1 (three walls - inlet, top, near side - have been hidden for clarity).

Contained within the overset cylinder is the propeller itself, using a "wall" boundary while the cylinder has an "overset" boundary to interface with the background. The entire overset region uses a polyhedral mesh, as shown in Figure 5-2, in order to capture the complex curvature of the propeller. A prism layer mesh is also enabled to improve the interface between the propeller wall and the overset cylinder. This figure also illustrates the necessary 5-cell overlap between the regions.

The collective mesh is shown in Figure 5-3. The mesh is densest around the propeller, with the cells growing at intervals radiating from the overset region around the propeller. The figure also shows the trimmed cell mesh of the background, which was beneficial to capturing the free surface since it is orthogonally aligned to the global reference frame. A final step in refining the mesh was the employment of two short boxes along the free surface (at $z = -0.061$ m, with the axis origin at the center of the shaft's aft edge), one nearer the propeller (with a finer mesh) and the other further downstream (with a coarser mesh), in order to aid the complex free-surface hydrodynamics. Similarly, a larger and longer cylinder was placed around the overset cylinder to assist in capturing the motion dynamics and resultant water spray. These refined mesh areas can be seen in both the centerline view of Figure 5-3 and the side boundary of Figure 5-1.

5.1.2 Physics Models

The following principal physics models were invoked to represent the complex multiphase hydrodynamics surrounding the propellers' operation on the free surface:

- Eulerian Multiphase (air and water phases present)
- Gravity
- Implicit Unsteady Flow
- K-Epsilon Turbulence
- Schnerr-Sauer Cavitation
- Realizable K-Epsilon Two-Layer
- Reynolds-Averaged Navier-Stokes
- Segregated Volume Flux-Based Flow
- Volume of Fluid (VOF) Wave

Together, these physics provided the basis for modeling turbulent, cavitating flow in a multiphase air-water environment on the free surface. The last item, VOF wave, served to model the advance speed as an incoming flat wave, with the speed adjusted in accordance with Table 5.1.

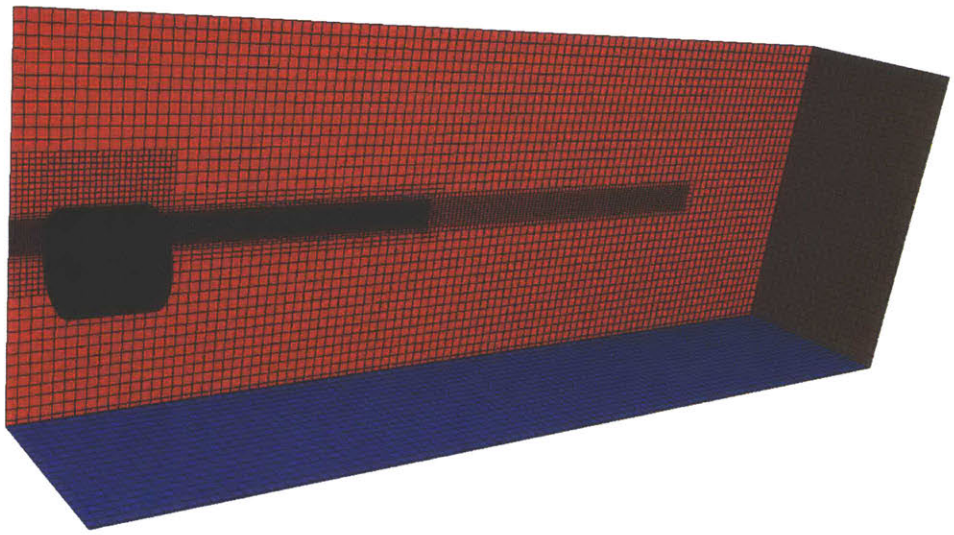

Figure 5-1: Background region with overset cylinder for CFD simulation (red = velocity inlet, blue = symmetry plane, tan = pressure outlet)

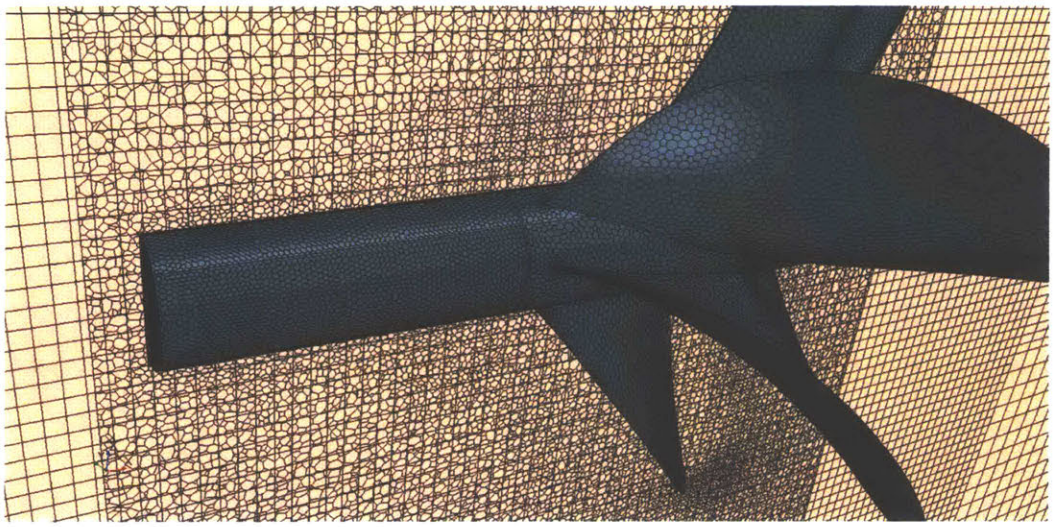

Figure 5-2: Overset region showing propeller discretization and interface between overset and background meshes

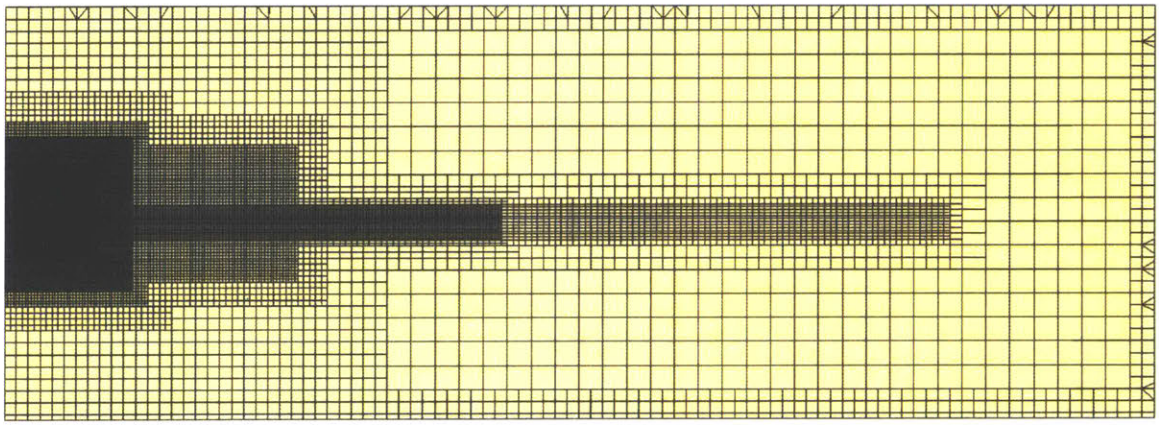

Figure 5-3: Mesh discretization across the simulation domain (centerline plane)

5.2 Discussion of Overall Flow Characteristics

As expected, supercavitating flow was observed on both propellers across the range of operating speeds. Overall, the *J5T* and baseline models exhibited similar flow characteristics. A review of the volume fractions of air scenes, which show the wetted state of the propeller (blue and red representing water and air, respectively, with vapor occupying the color spectrum in between), serve to illustrate the typical performance characteristics of surface-piercing, supercavitating blades. As defined by Young and Kinnas, such propellers operate in three regimes [39]:

> **Partially-Ventilated Regime**: The air cavities start near the blunt trailing edge and vent toward the free surface. When the advance coefficient is reduced, a partial cavity filled primarily with liquid vapor may also develop. In this flow regime, the extent and volume of the air cavity, as well as the time-averaged thrust and torque coefficients, tend to increase with decreasing advance coefficient.
>
> **Transition Regime**: When the advance coefficient is further reduced from the partially-ventilated regime, the propeller enters the transition regime. This flow regime is highly unstable, and is accompanied by violent oscillatory forces. The air cavities will start to spread toward the blade leading edge and fluctuate in shape and size. In addition, a sudden drop in thrust and torque coefficients will occur due to spread of air cavities toward blade leading edge.
>
> **Fully-Ventilated Regime**: When the advance coefficient is further reduced, the propeller enters the fully-ventilated regime. This flow regime is characterized by continuous ventilated cavities that start near the leading edge on the suction side of each blade and vent to the atmosphere. This flow regime is relatively stable and the blade trailing edge remains ventilated at all times. The thrust and torque coefficients tend to decrease with the advance coefficient due to the dominance of cascade effects.

Figure 5-4 shows the propellers operating in the partially-ventilated regime at the baseline advance ratio. Although the forward non-pressure surfaces (upper images) are mostly red, indicating that they are operating in a vapor/ventilation cavity, they are nevertheless partially wet. The *J5T* propeller shows greater wetted area on this surface concentrated towards the hub, whereas the baseilne propeller's wetted area is slightly more limited to the leading edge. The aft views of the pressure faces (lower images) instead show a majority of wetted area as designed, although small pockets of

air exist. Notably, the *SCSB* tail section of the *J5T* propeller remains red, indicating that it successfully remains within the cavity without flow interference.

Despite the wetted forward surfaces, the surface pressure view of Figure 5-5 reveals that these wetted areas had little measurable impact in terms of pressure. The upper images illustrate that the non-pressure surfaces have negligible pressure across them, as expected. The lower images instead demonstrate that the pressure faces act as the source of thrust for the propellers, with the preponderance of pressure concentrated around the trailing edge of these surfaces.

Alternately, Figure 5-6 shows the significantly different flow characteristics, with the propellers operating in the fully-ventilated regime at half the baseline advance ratio. The upper images show forward non-pressure surfaces almost completely free of wetted areas, while the lower images show fully wet pressure surfaces (these surfaces also remain wet as they exit the water above the free surface due to carrying the water on the blades). This is not unexpected behavior however, and the pressure view of Figure 5-7 shows overall similar performance as on Figure 5-5.

The collective results of thrust and torque are presented in Figures 5-8 and 5-9 (*note: the axis convention for $+x$ is against the flow, such that a positive torque is in the same direction as the counter-clockwise propeller rotation; for this reason, the torque values are negative*). These plots display the differences between the flow regimes: as the lower values of J appear to result in fully-ventilated operation, the thrust and torque are consequently significantly reduced. Meanwhile, the simulations at the baseline J exhibit significantly higher performance values in the partially-ventilated regime.

In order to develop a more detailed comparison of thrust and torque, the simulations are analyzed independently in Section 5.3. For these analyses, the thrust and torque for the entire propeller were used, averaged across a specified time range, rather than evaluating individual blades. Each blade was however monitored individually, as shown in Figures 5-10 and 5-11.

These figures illustrate the comparatively unsteady nature of the blade performance profiles versus the total propeller performance profiles of the following section. Particularly after the flow discontinuity (discussed in Section 5.2.1), the blades exhibit inconsistent behavior; on the contrary, relatively steady solutions could be gleaned from the total thrust and torque profiles of Section 5.3, where the effect of such

inconsistencies was minimized when taking the average.

Furthermore, Figures 5-10 and 5-11 serve to display the unsteady nature of the thrust and torque inherent to surface-piercing propellers. In each blade period, an initial sharp rise is observed resulting from the forward edge of the blade entering the water at high speed. This peak is followed by a gradual decline where the blade is submerged. When the blade begins to exit the water, the result is an unsteady effect on the thrust and torque that produces irregular fluctuations in the data. This performance profile is consistent with prior experiments on surface-piercing propellers [26].

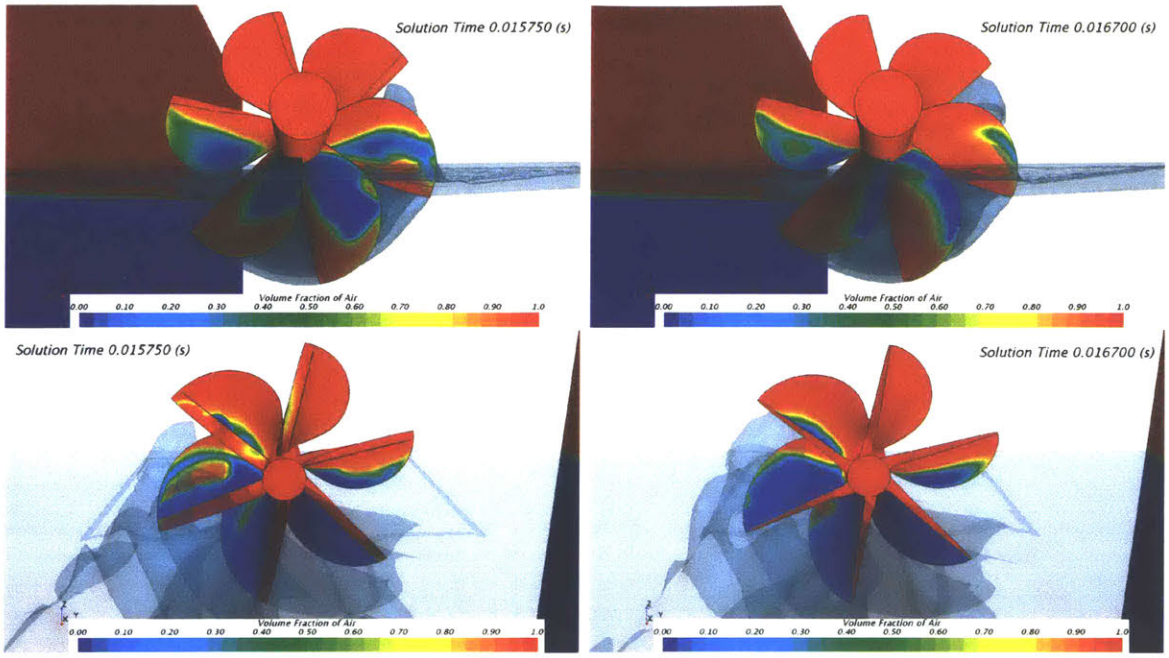

(a) *J5T* Propeller (b) Baseline Propeller

Figure 5-4: Volume fractions of air for the *J5T* and baseline propellers operating at the baseline advance ratio

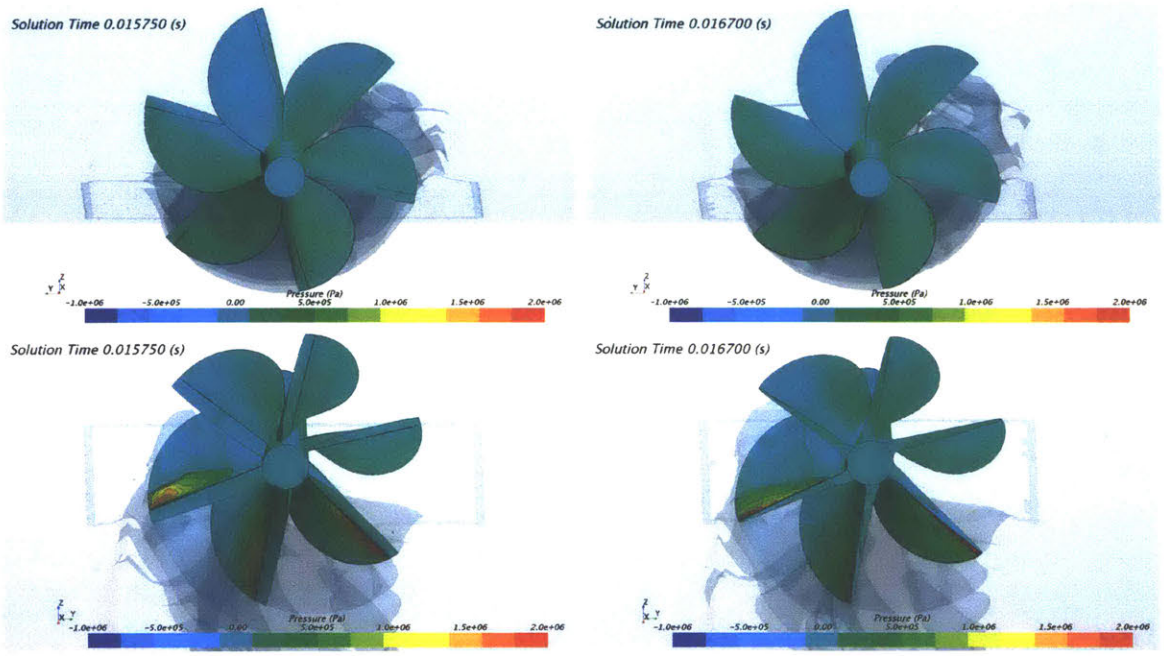

(a) *J5T* Propeller (b) Baseline Propeller

Figure 5-5: Surface pressure on the *J5T* and baseline propellers operating at the baseline advance ratio

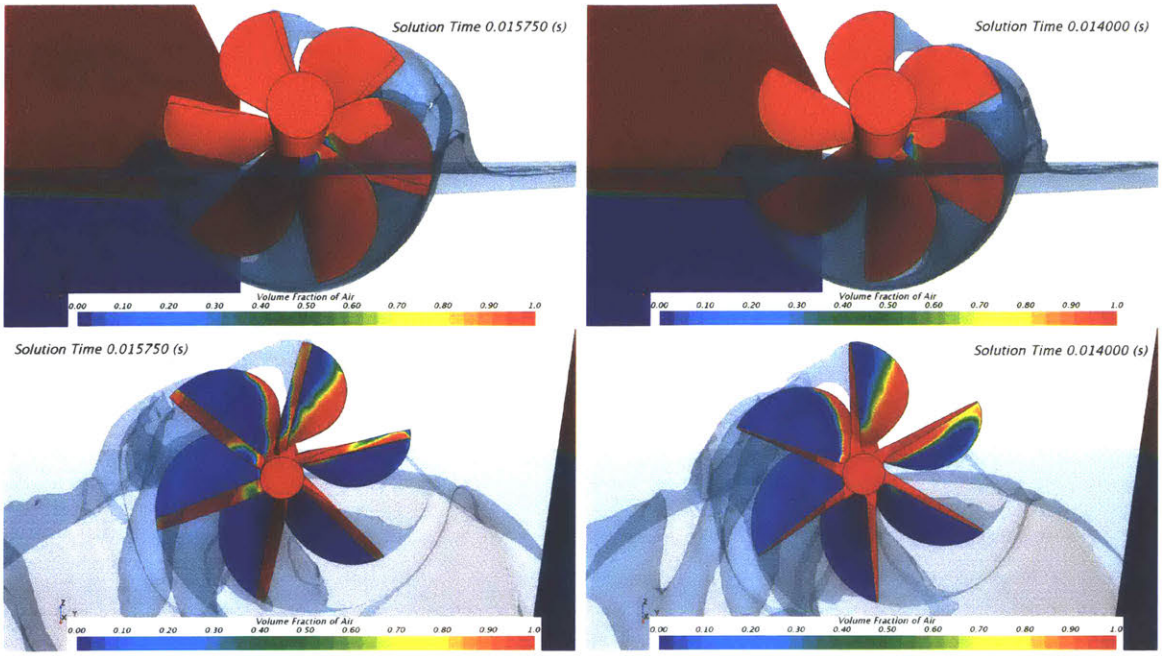

(a) *J5T* Propeller (b) Baseline Propeller

Figure 5-6: Volume fractions of air for the *J5T* and baseline propellers operating at 1/2 advance ratio

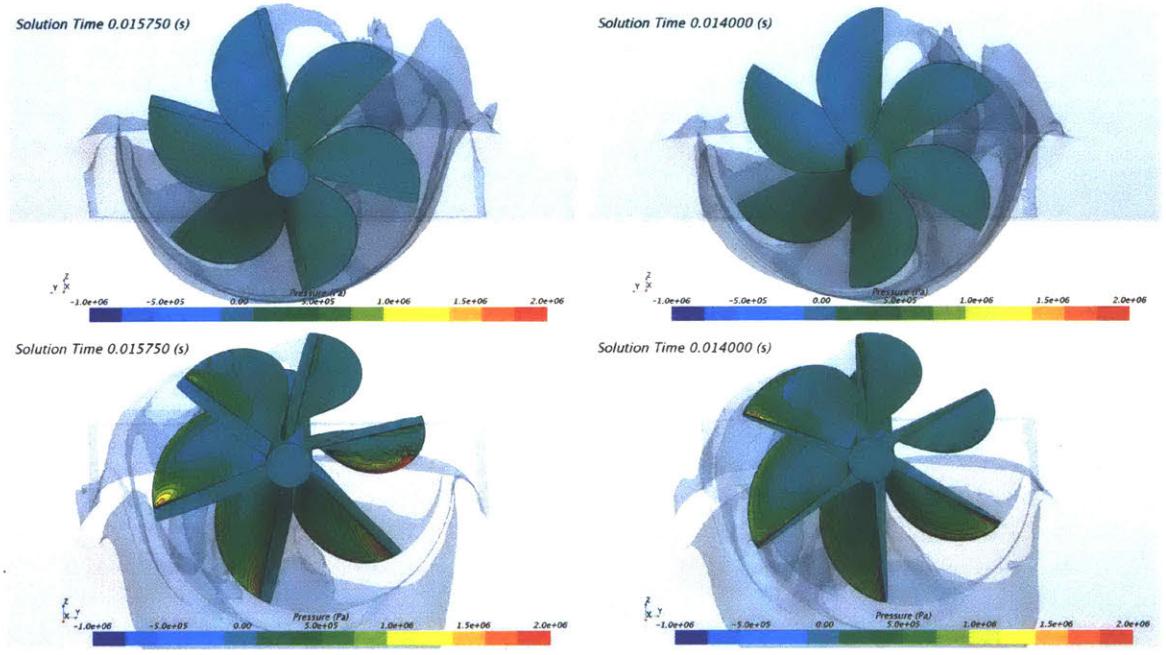

(a) *J5T* Propeller (b) Baseline Propeller

Figure 5-7: Surface pressure on the *J5T* and baseline propellers operating at 1/2 advance ratio

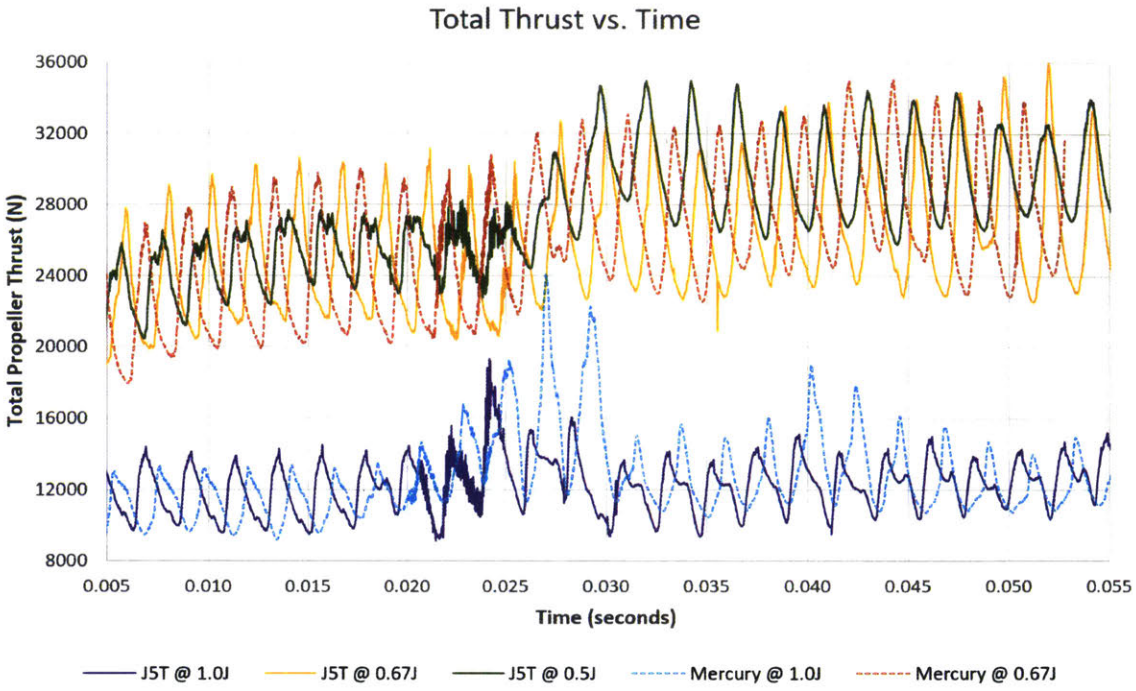

Figure 5-8: Thrust vs. time for all simulations

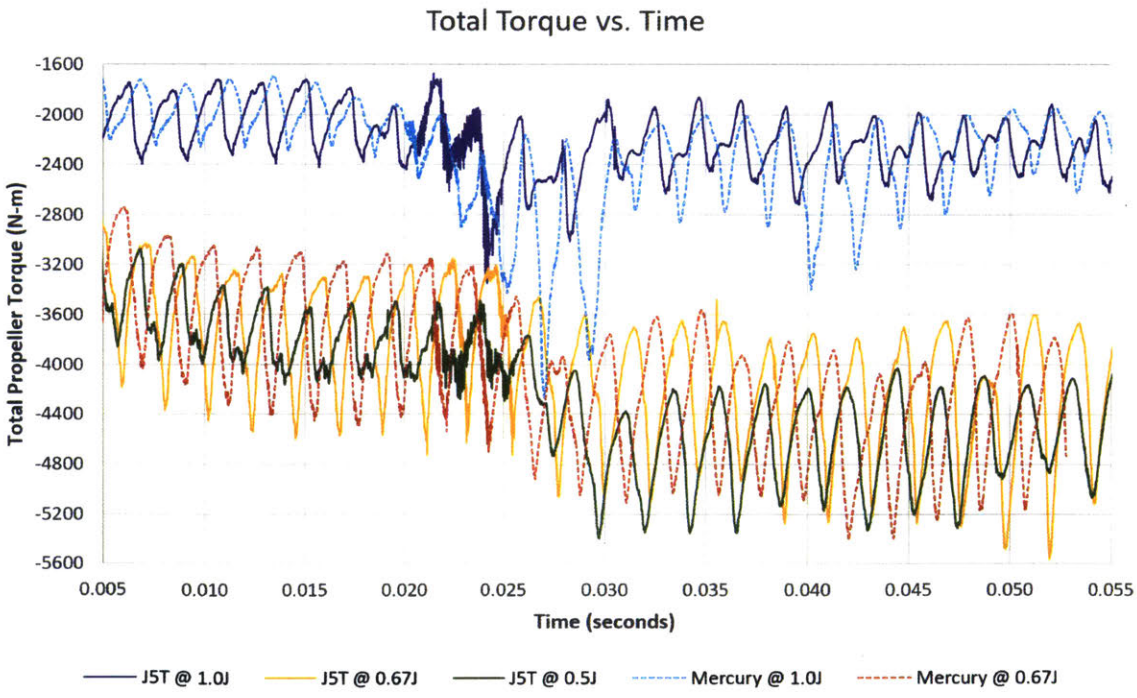

Figure 5-9: Torque vs. time for all simulations

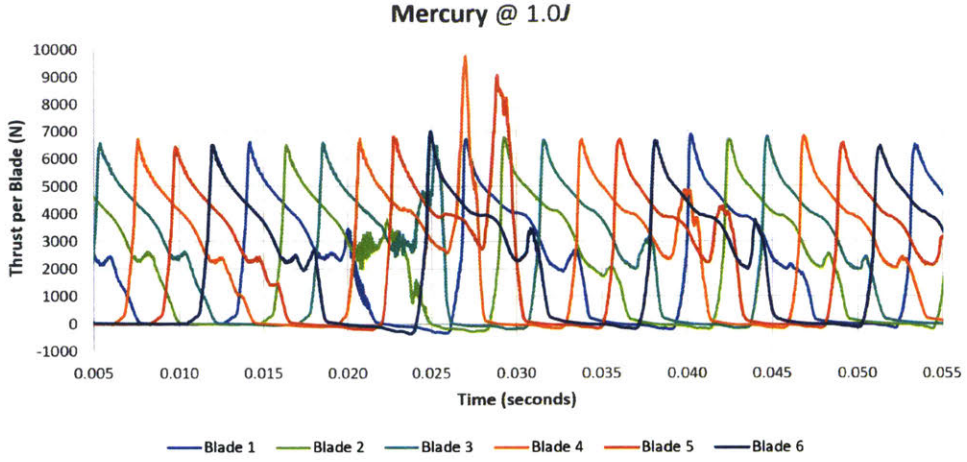

(a) Thrust per blade over duration of simulation

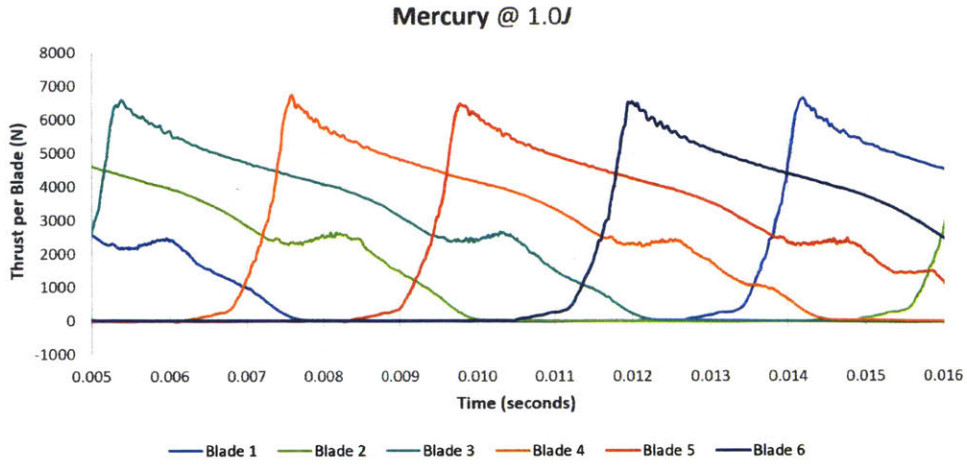

(b) Selected region before discontinuity

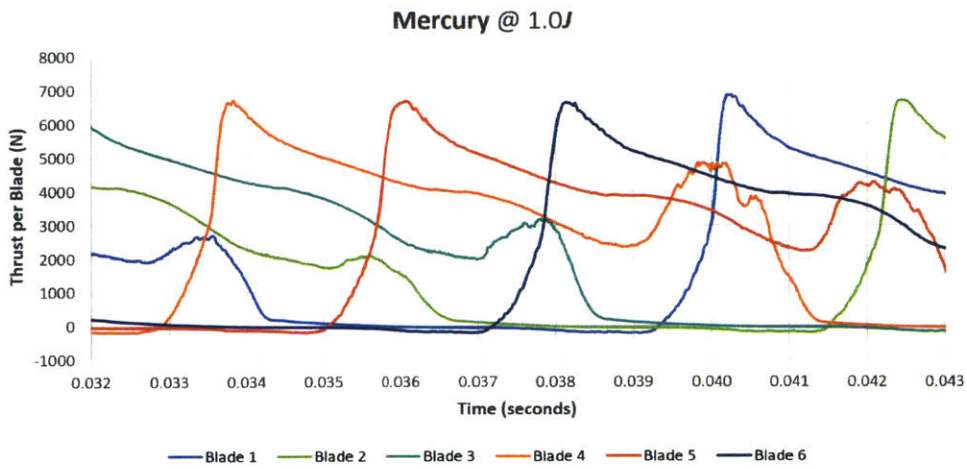

(c) Selected region after discontinuity

Figure 5-10: Baseline thrust per blade at baseline advance ratio

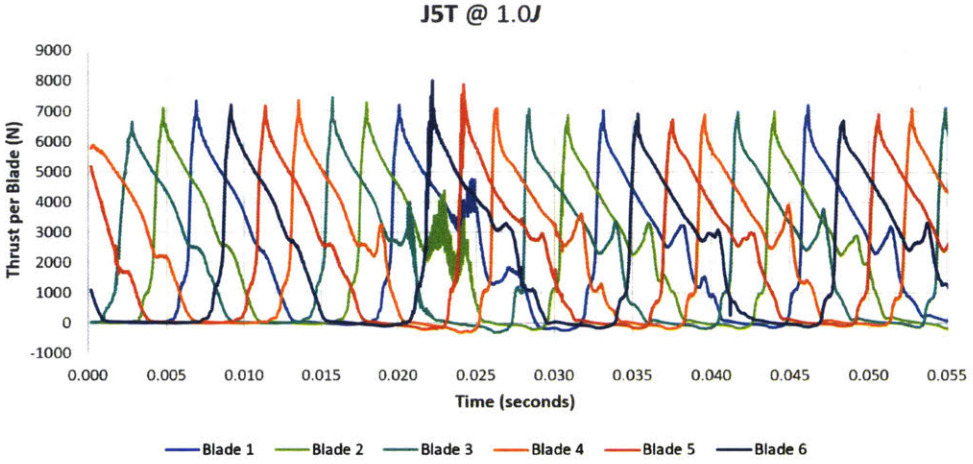

(a) Thrust per blade over duration of simulation

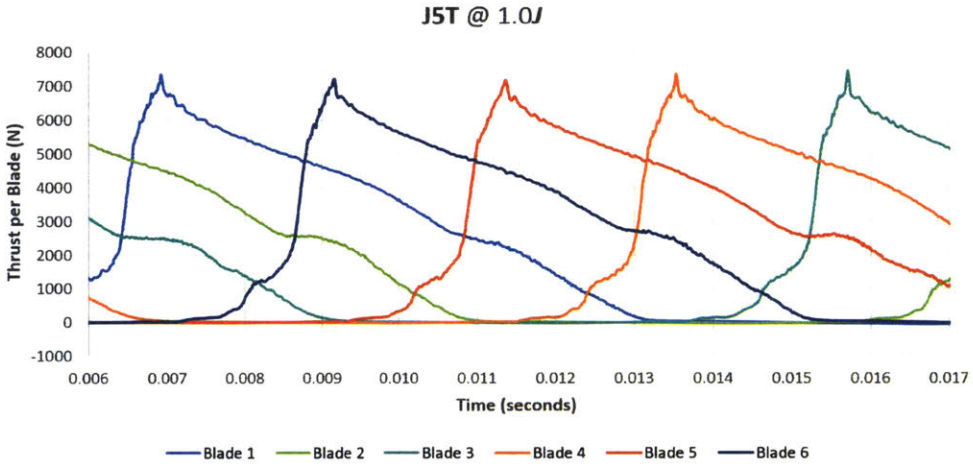

(b) Selected region before discontinuity

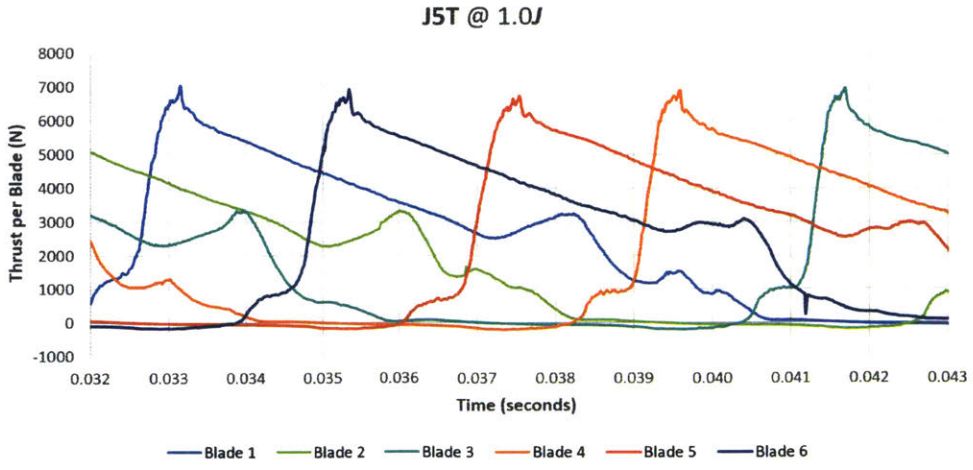

(c) Selected region after discontinuity

Figure 5-11: J5T thrust per blade at baseline advance ratio

5.2.1 Flow Discontinuity

A peculiarity of the simulations was a discontinuity in the flow approximately two-thirds into the simulation runtime. This discontinuity was repeated in each of the simulations, for both propellers across the range of advance ratios, commencing each time around 0.020 seconds. Visually, this phenomenon appears in concert with a large trough developing in the flow aft of the propeller, with a sharp crest rising on the port side. This transient event is the result of the impulsive flow simulation start: the simulation is initialized with the propeller running at full RPM while the free surface flows with uniform, flat velocity throughout the whole domain (including the region close to the rotating blades). An example of this visualization is provided in Figure 5-12, showing the free surface of the $J5T$ simulation running at the baseline advance ratio. The other simulations for both propellers presented similar manifestations of this transient free surface disturbance.

The effect of this phenomenon can be readily observed in the thrust and torque results of Section 5.3, to varying degrees. Despite the abrupt initialization of the flow, the numerical computation shows a relatively stabilized periodic force signal in the leading five or six blade periods. This corresponds to the predicted flow with a distinct hollow behind the propeller. In each case, the flow shows a collapse of the free surface sheet risen by the propeller action onto the wave trough created in the wake of the propeller at around 0.020-0.025 seconds, followed by an overall change in the thrust and torque results. In some cases a significant change is witnessed, such as on the $J5T$ simulation running at $0.5J$ where a substantial increase in torque and thrust occurs (Figures 5-21 and 5-24). On the other hand, the $J5T$ simulation running at the baseline advance ratio sees a large spike at the discontinuity but a less appreciable change in the results thereafter (Figures 5-19 and 5-22). On the whole, the solutions appear to be steadier (peaks of similar amplitude and shape) before the discontinuity. At the same time, the solutions appear smoother after the discontinuity.

The steady flow regime of a surface-piercing propeller in real-world operation is expected to correspond to the second steady-state regime observed during the numerical simulations. However, the effect of the change in mesh resolution in the vicinity of the wake where the wave trough created by the propeller first starts to seal up during the transient simulation has not be fully addressed; although a limited mesh sensitivity analysis was conducted to determine the final mesh configuration,

the time frame of this thesis prohibited an extensive mesh analysis. Therefore, the solutions both *before* and *after* the discontinuous region are analyzed in the ensuing sections, where periods of apparent steady-state operation were selected. Although the discontinuity has an evident effect on the results, the *relative* effect for the comparative analysis of the two propellers appears to be minimal.

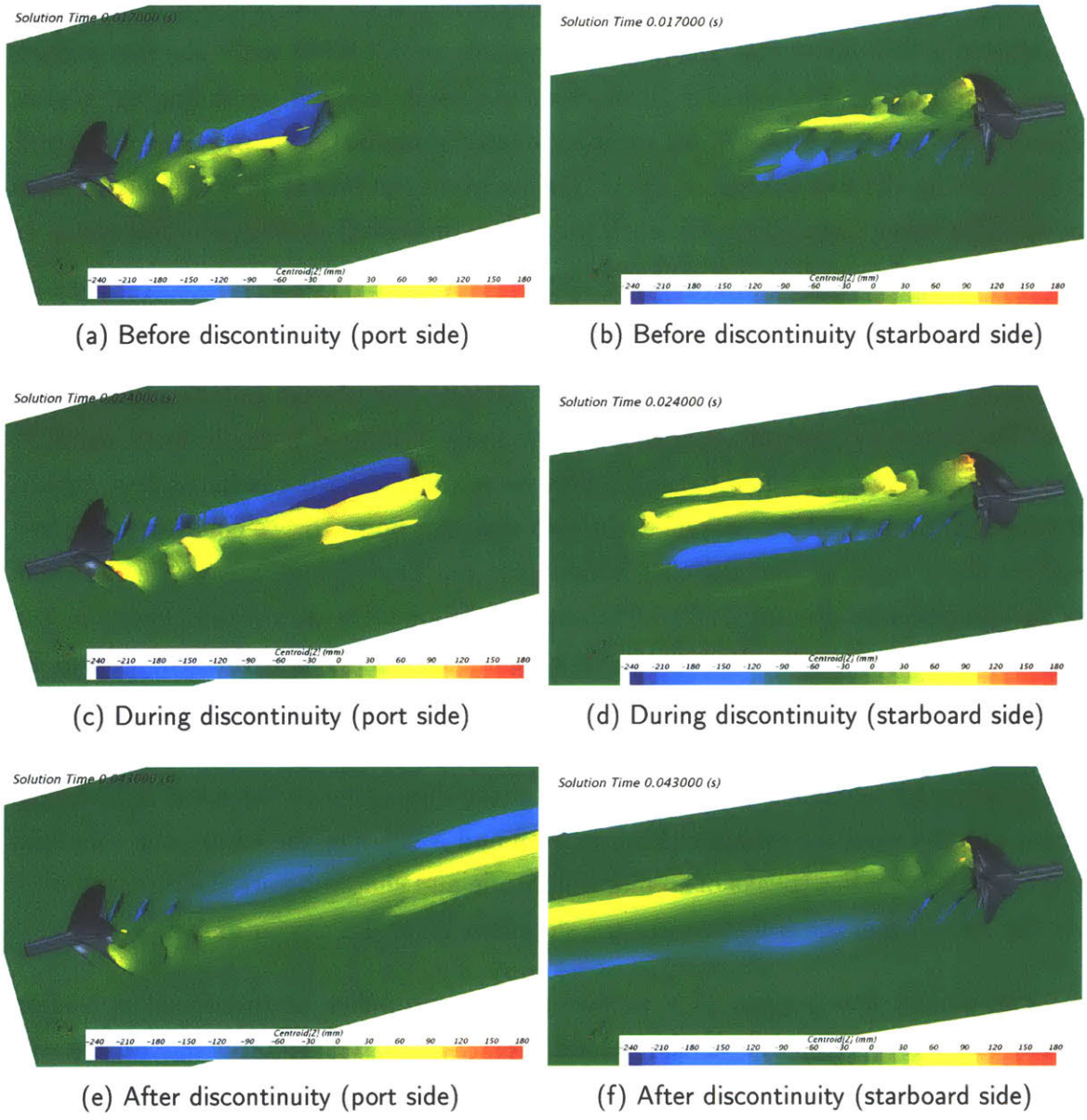

(a) Before discontinuity (port side)

(b) Before discontinuity (starboard side)

(c) During discontinuity (port side)

(d) During discontinuity (starboard side)

(e) After discontinuity (port side)

(f) After discontinuity (starboard side)

Figure 5-12: Free surface view of *J5T* propeller running at baseline advance ratio showing time before, during, and after flow discontinuity

5.3 Thrust and Torque Results

The thrust and torque were analyzed for both propellers across the range of advance ratios in accordance with Table 5.1. The results were parsed into regions *before* and *after* the discontinuity addressed in Section 5.2.1 in order to assess the changes to the steady-state solutions. The full results of each simulation, including the selected regions on either side of the discontinuity, are provided in Figures 5-13 through 5-24.

The averaged results from before and after the discontinuity are listed in Tables 5.2 and 5.3, respectively. The thrust and torque data from the simulations were translated in to thrust and torque coefficients K_T and K_Q by the following relations:

$$K_T = \frac{T}{\rho n^2 d^4} \tag{5.2}$$

$$K_Q = \frac{Q}{\rho n^2 d^5} \tag{5.3}$$

As the ultimate measure of overall performance, the open-water propeller efficiency η_p was calculated as follows:

$$\eta_p = \frac{J}{2\pi}\frac{K_T}{K_Q} \tag{5.4}$$

Table 5.2: Thrust and torque results from 3D CFD simulations (***before*** *discontinuity*)

Parameter	*Symbol*	*Values*			*Units*
J Multiplication Factor		1	0.667	0.5	-
Advance Ratio	J	1.767	1.178	0.884	-
Advance Speed	V_a	58.115	38.743	29.058	m/s
Thrust ($J5T$)	T_{J5T}	11196	24529	25290	N
Thrust (Baseline)	T_{base}	11146	23900	25074	N
Thrust Coefficient ($J5T$)	$K_{T(J5T)}$	0.0557	0.122	0.126	-
Thrust Coefficient (Baseline)	$K_{T(base)}$	0.0554	0.119	0.125	-
Torque ($J5T$)	Q_{J5T}	1940	3714	3810	N-m
Torque (Baseline)	Q_{base}	1951	3622	3755	N-m
Torque Coefficient ($J5T$)	$K_{Q(J5T)}$	0.0223	0.0428	0.0439	-
Torque Coefficient (Baseline)	$K_{Q(base)}$	0.0225	0.0417	0.0432	-
Propeller Efficiency ($J5T$)	$\eta_{p(J5T)}$	0.701	0.535	0.403	-
Propeller Efficiency (Baseline)	$\eta_{p(base)}$	0.694	0.534		-

Table 5.3: Thrust and torque results from 3D CFD simulations (***after*** *discontinuity*)

Parameter	*Symbol*	*Values*			*Units*
J Multiplication Factor		1	0.667	0.5	-
Advance Ratio	J	1.767	1.178	0.884	-
Advance Speed	V_a	58.115	38.743	29.058	m/s
Thrust ($J5T$)	T_{J5T}	12139	26356	29965	N
Thrust (Baseline)	T_{base}	13034	27397	30031	N
Thrust Coefficient ($J5T$)	$K_{T(J5T)}$	0.0604	0.131	0.149	-
Thrust Coefficient (Baseline)	$K_{T(base)}$	0.0648	0.136	0.149	-
Torque ($J5T$)	Q_{J5T}	2255	4154	4666	N-m
Torque (Baseline)	Q_{base}	2411	4314	4608	N-m
Torque Coefficient ($J5T$)	$K_{Q(J5T)}$	0.026	0.0478	0.0537	-
Torque Coefficient (Baseline)	$K_{Q(base)}$	0.0278	0.0497	0.0531	-
Propeller Efficiency ($J5T$)	$\eta_{p(J5T)}$	0.654	0.514	0.390	-
Propeller Efficiency (Baseline)	$\eta_{p(base)}$	0.656	0.514		-

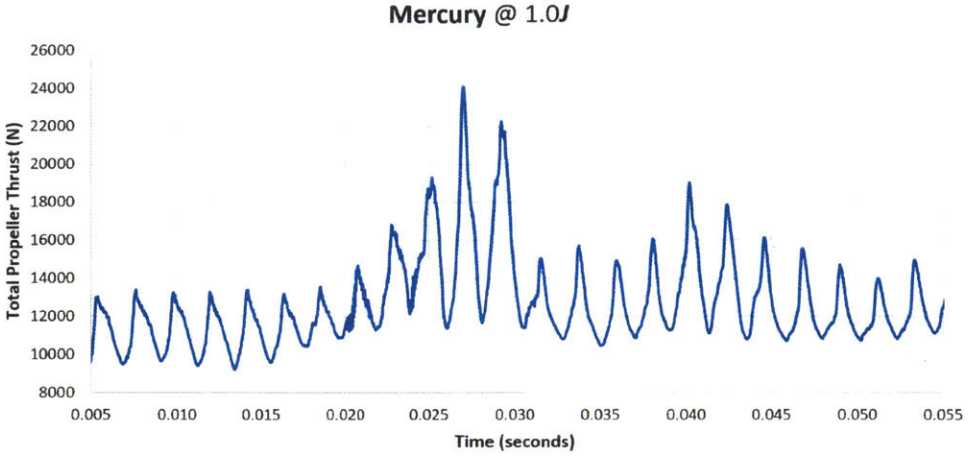

(a) Total thrust profile over duration of simulation

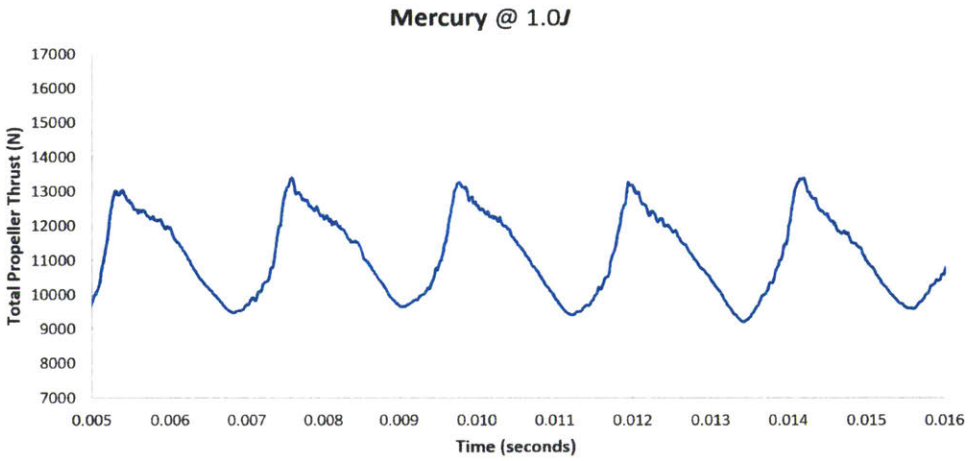

(b) Selected region before discontinuity

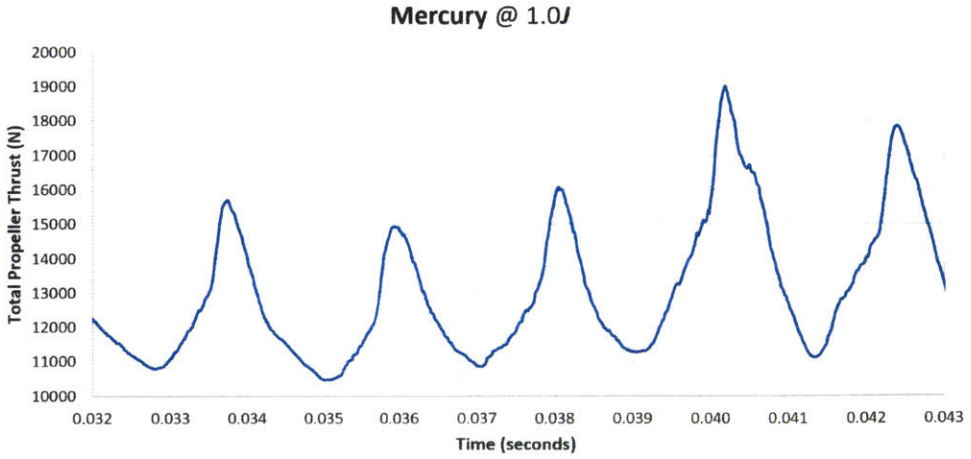

(c) Selected region after discontinuity

Figure 5-13: Total Thrust at Baseline Advance Ratio for Baseline Propeller

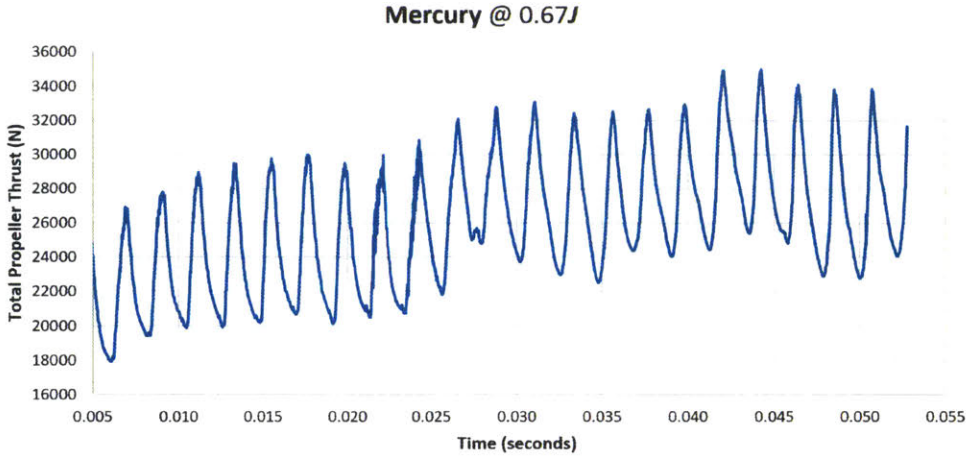

(a) Total thrust profile over duration of simulation

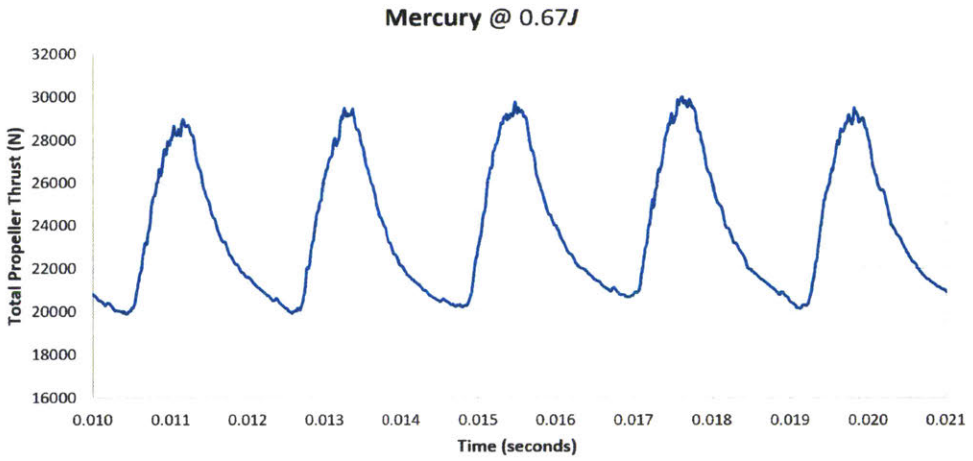

(b) Selected region before discontinuity

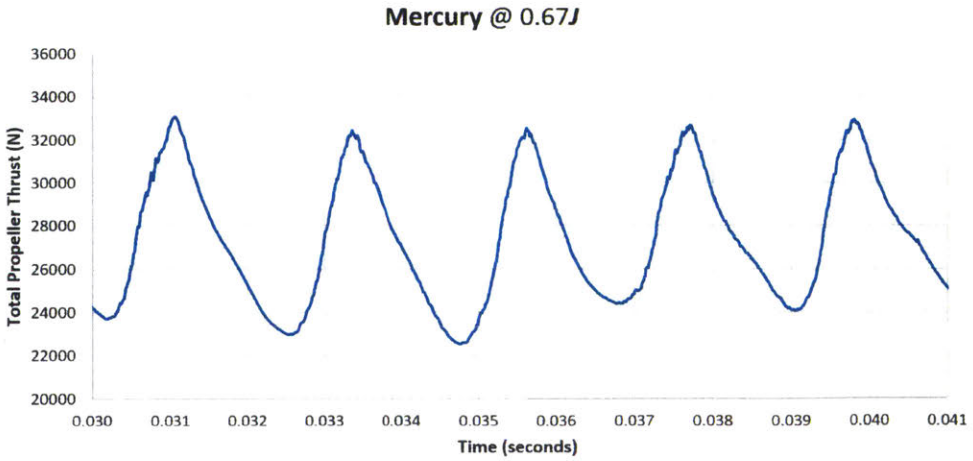

(c) Selected region after discontinuity

Figure 5-14: Total Thrust at 2/3 Advance Ratio for Baseline Propeller

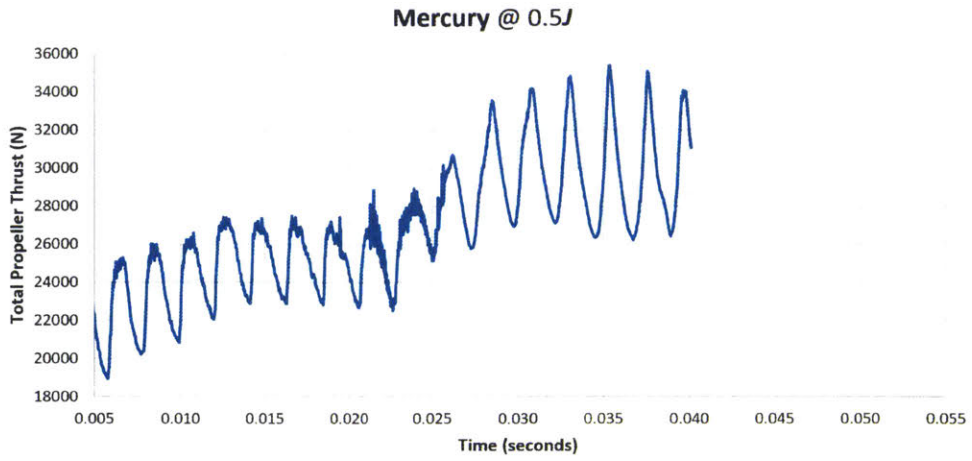

(a) Total thrust profile over duration of simulation

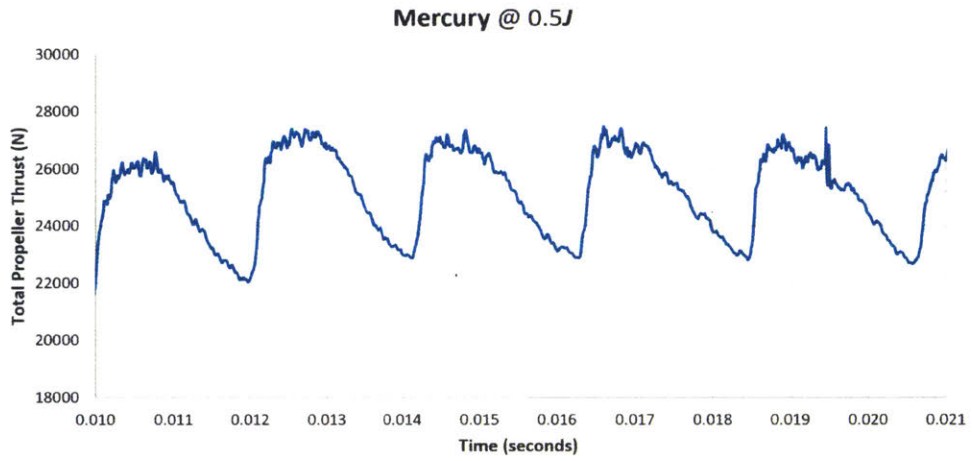

(b) Selected region before discontinuity

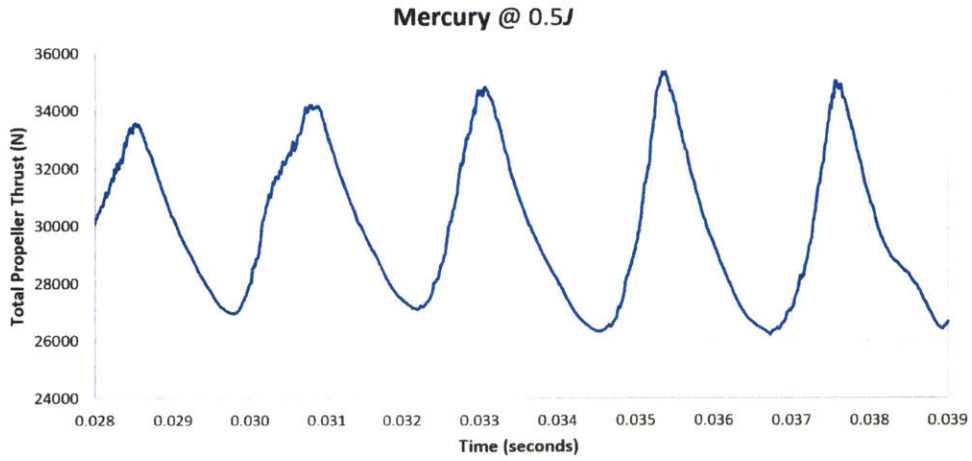

(c) Selected region after discontinuity

Figure 5-15: Total Thrust at 1/2 Advance Ratio for Baseline Propeller

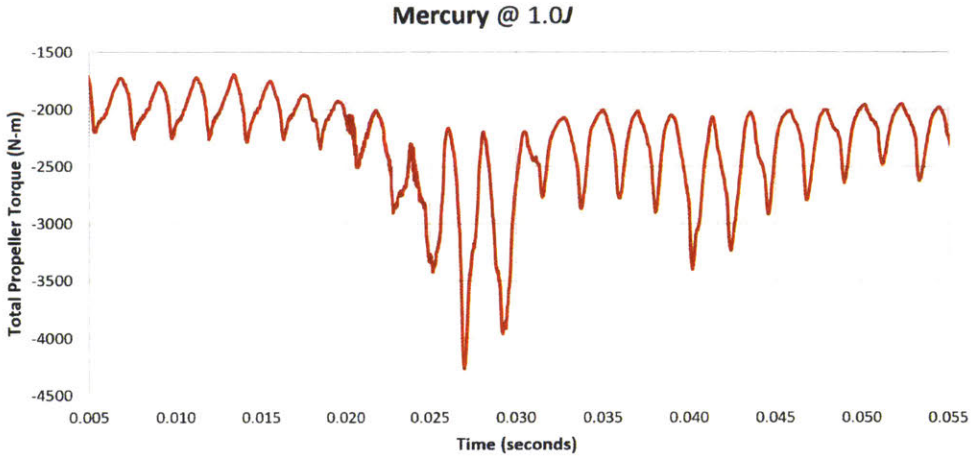

(a) Total torque profile over duration of simulation

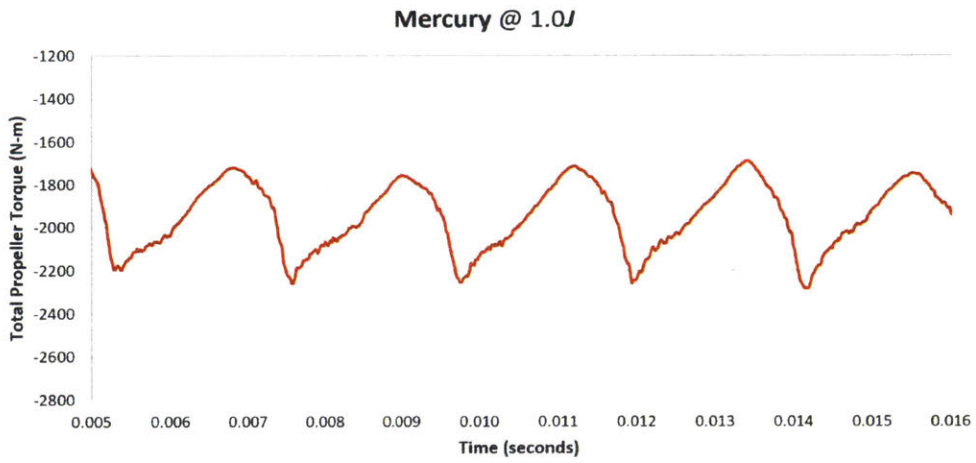

(b) Selected region before discontinuity

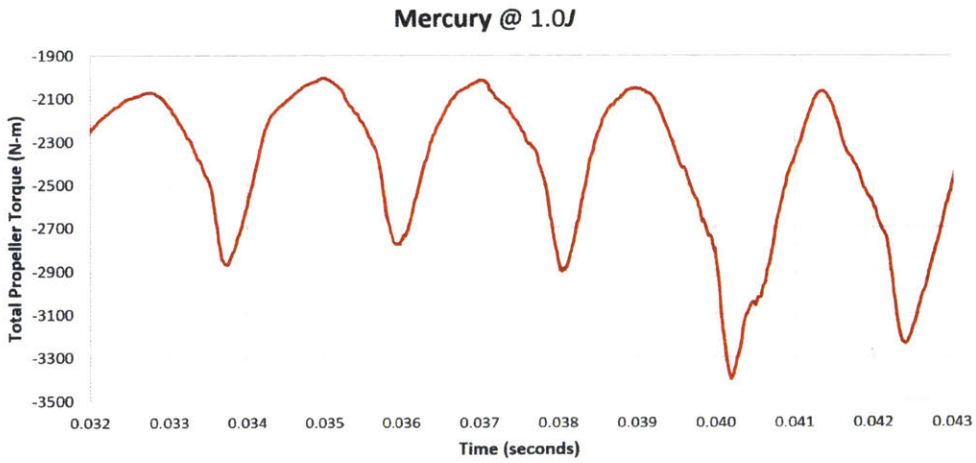

(c) Selected region after discontinuity

Figure 5-16: Total Torque at Baseline Advance Ratio for Baseline Propeller

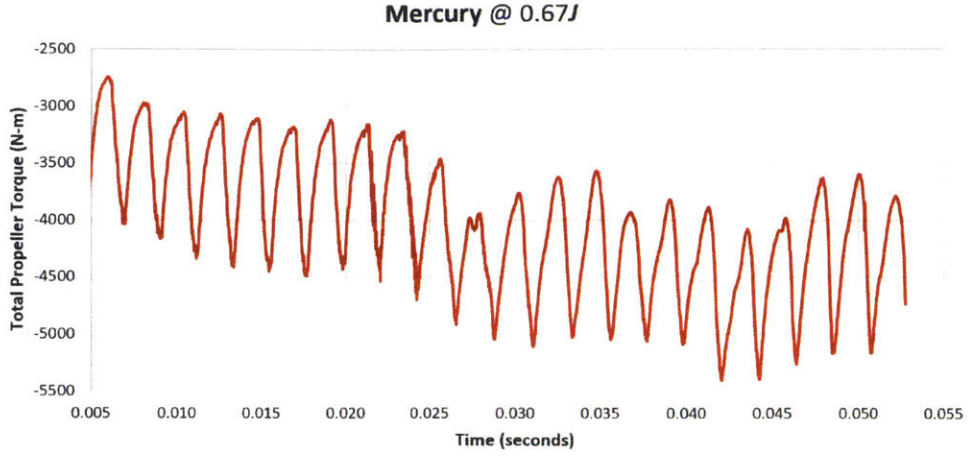

(a) Total torque profile over duration of simulation

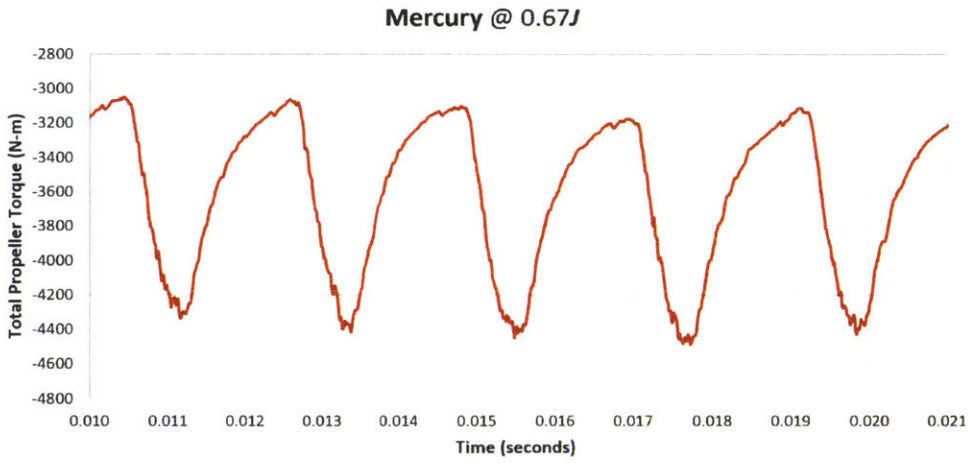

(b) Selected region before discontinuity

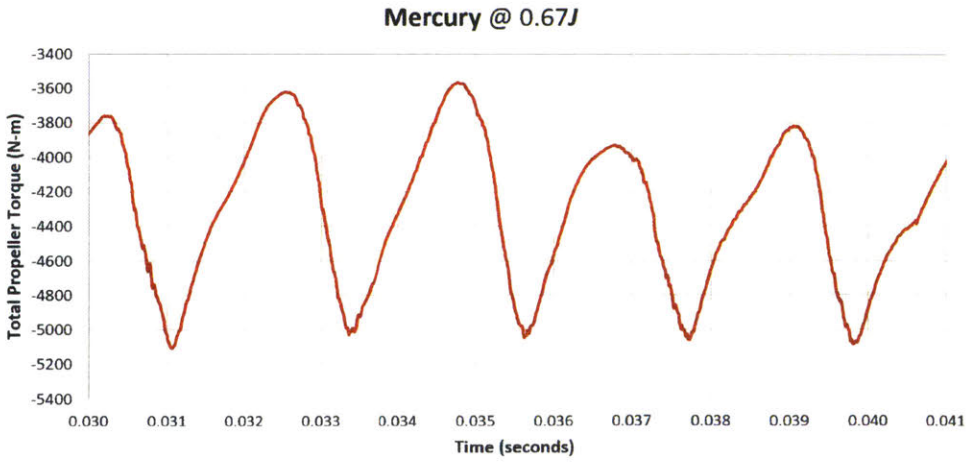

(c) Selected region after discontinuity

Figure 5-17: Total Torque at 2/3 Advance Ratio for Baseline Propeller

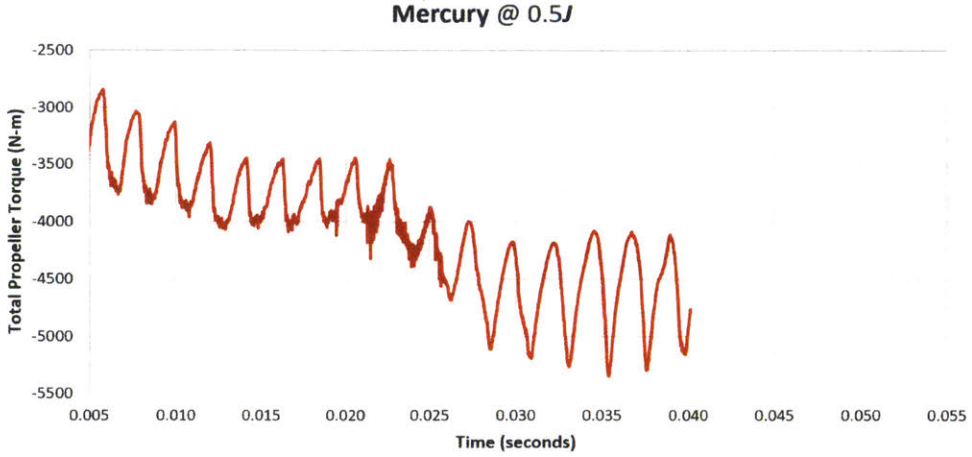

(a) Total torque profile over duration of simulation

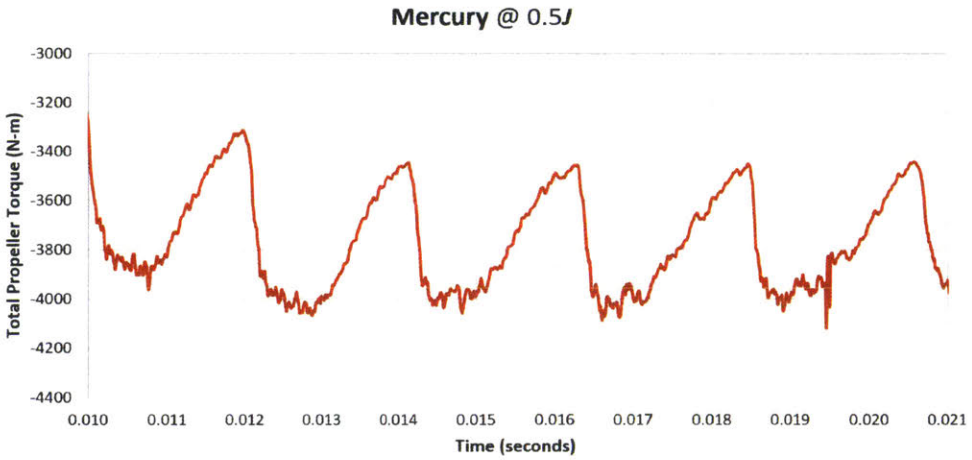

(b) Selected region before discontinuity

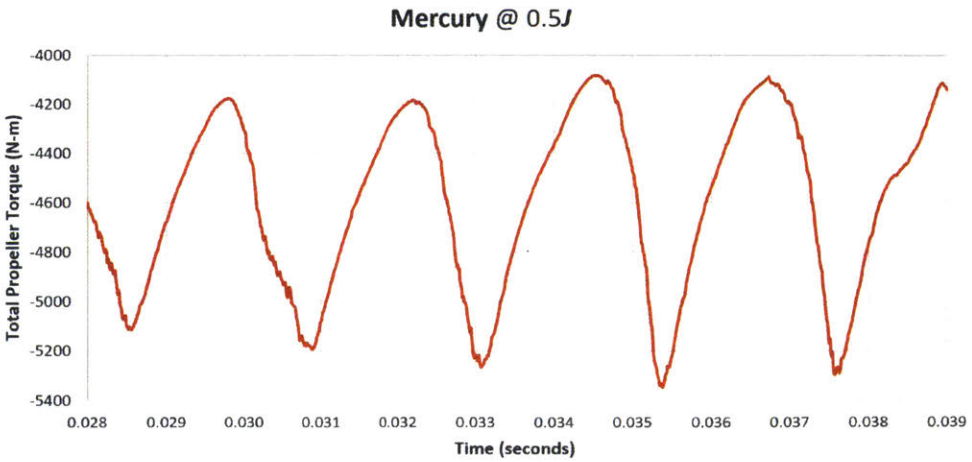

(c) Selected region after discontinuity

Figure 5-18: Total Torque at 1/2 Advance Ratio for Baseline Propeller

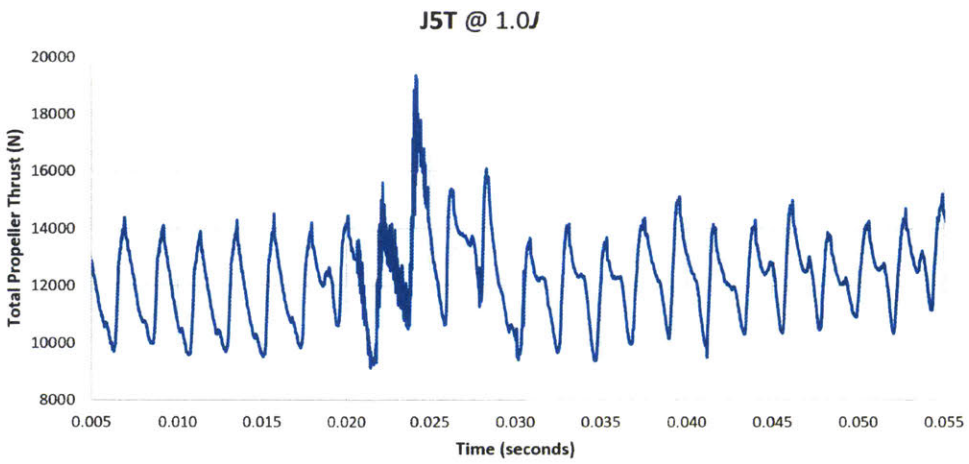

(a) Total thrust profile over duration of simulation

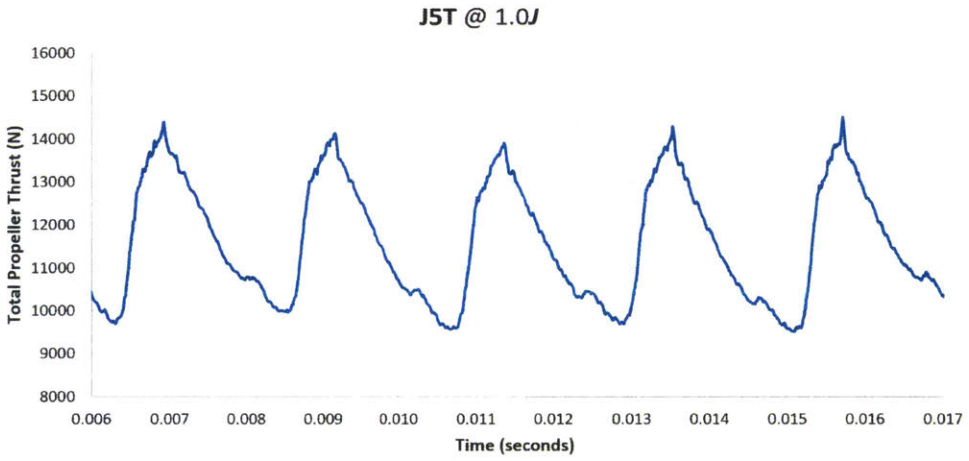

(b) Selected region before discontinuity

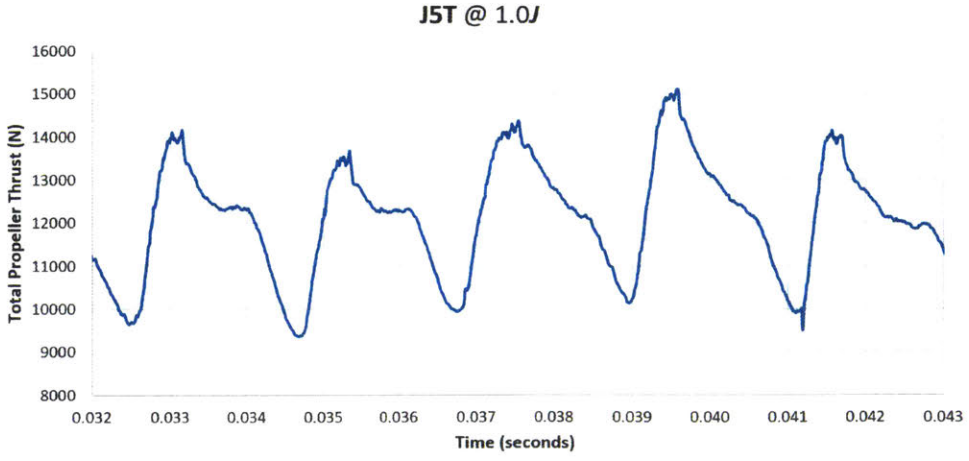

(c) Selected region after discontinuity

Figure 5-19: Total Thrust at Baseline Advance Ratio for *J5T* Propeller

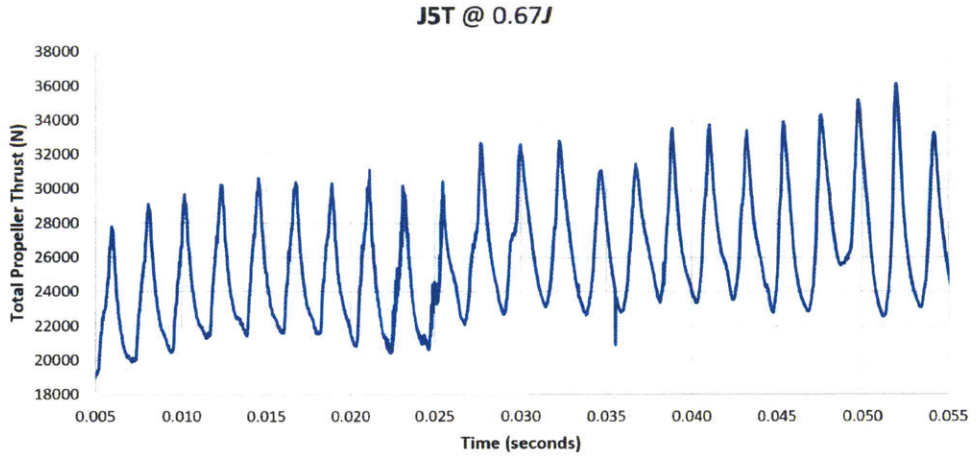

(a) Total thrust profile over duration of simulation

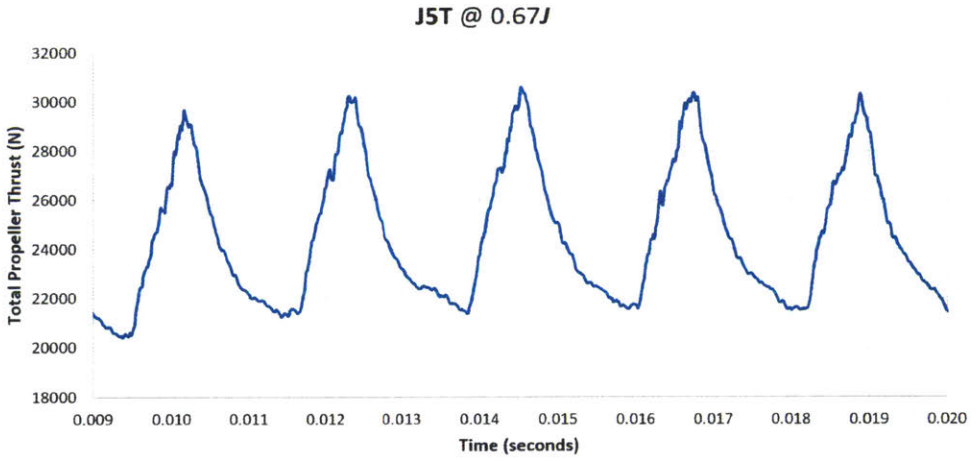

(b) Selected region before discontinuity

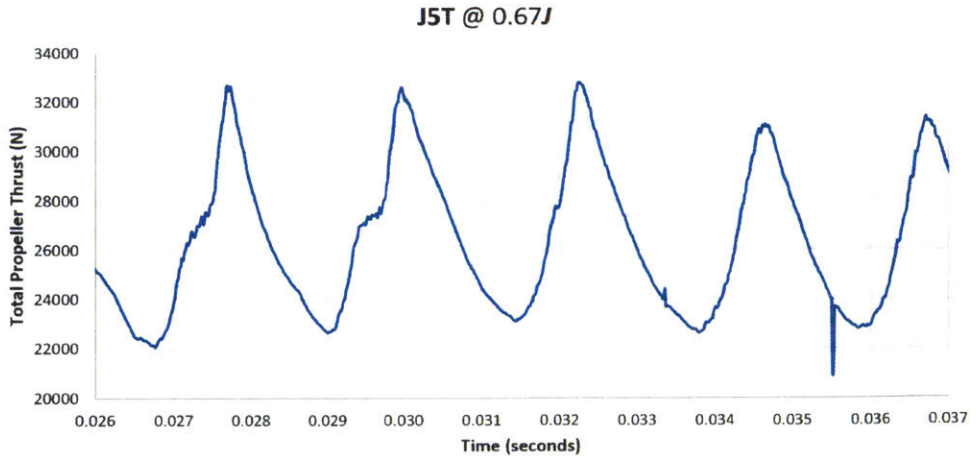

(c) Selected region after discontinuity

Figure 5-20: Total Thrust at 2/3 Advance Ratio for *J5T* Propeller

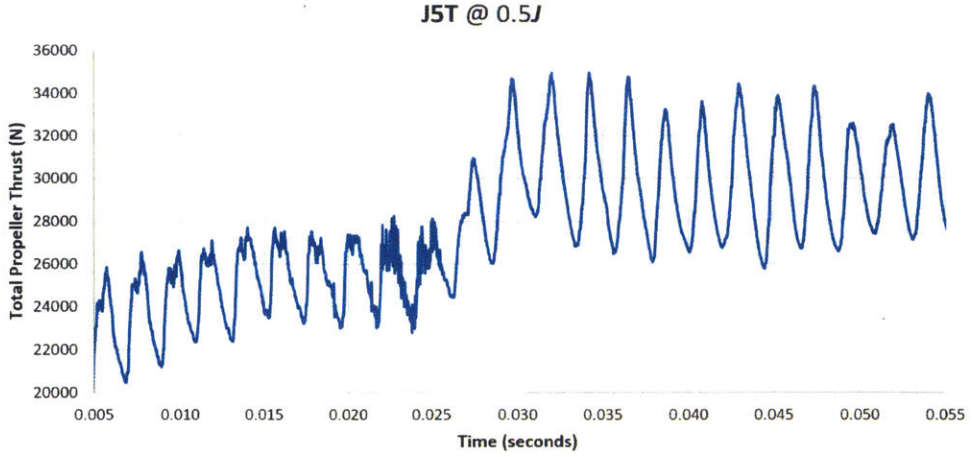

(a) Total thrust profile over duration of simulation

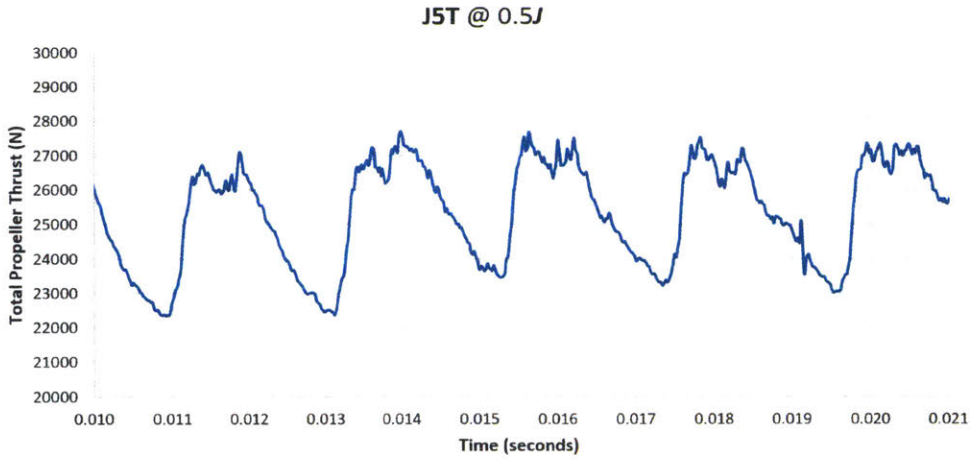

(b) Selected region before discontinuity

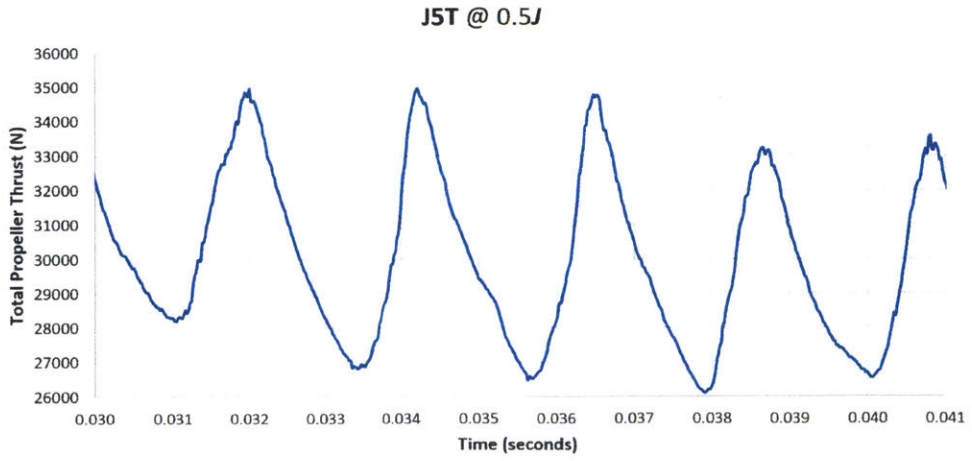

(c) Selected region after discontinuity

Figure 5-21: Total Thrust at 1/2 Advance Ratio for *J5T* Propeller

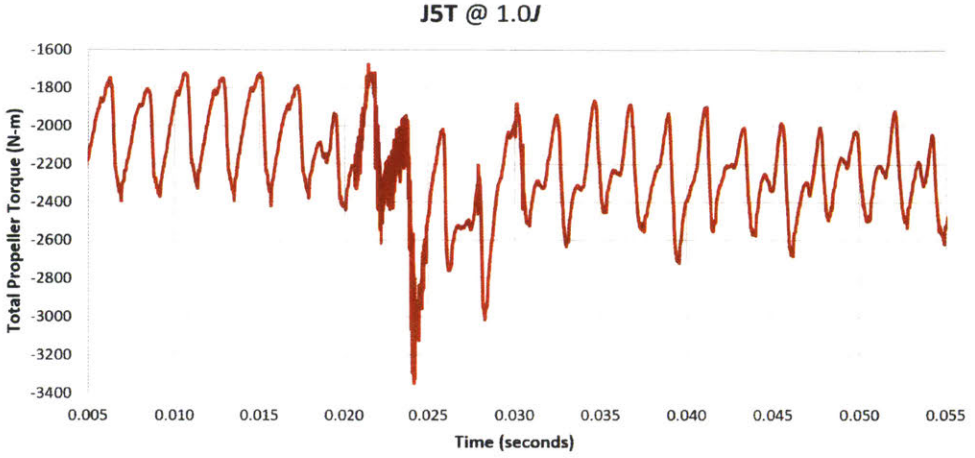

(a) Total torque profile over duration of simulation

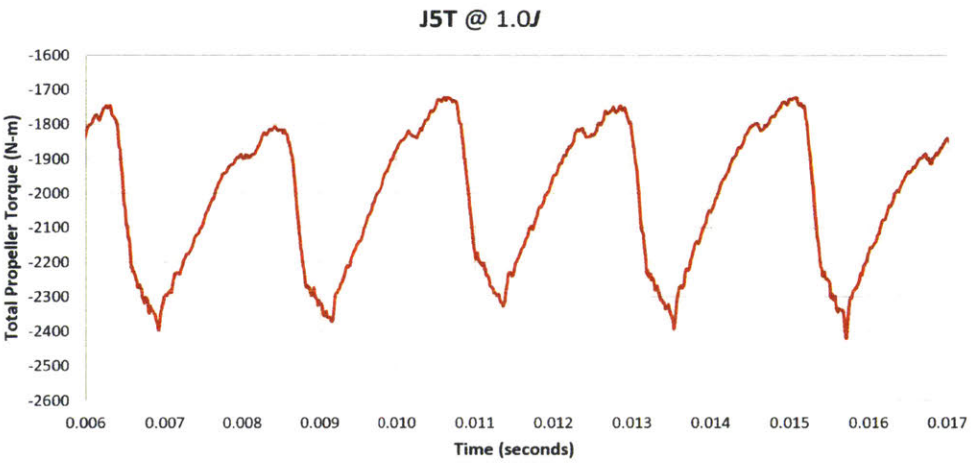

(b) Selected region before discontinuity

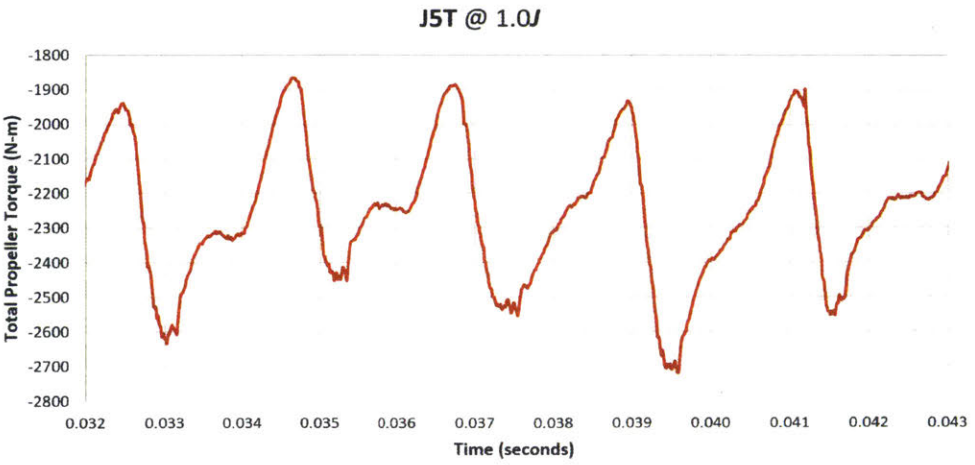

(c) Selected region after discontinuity

Figure 5-22: Total Torque at Baseline Advance Ratio for *J5T* Propeller

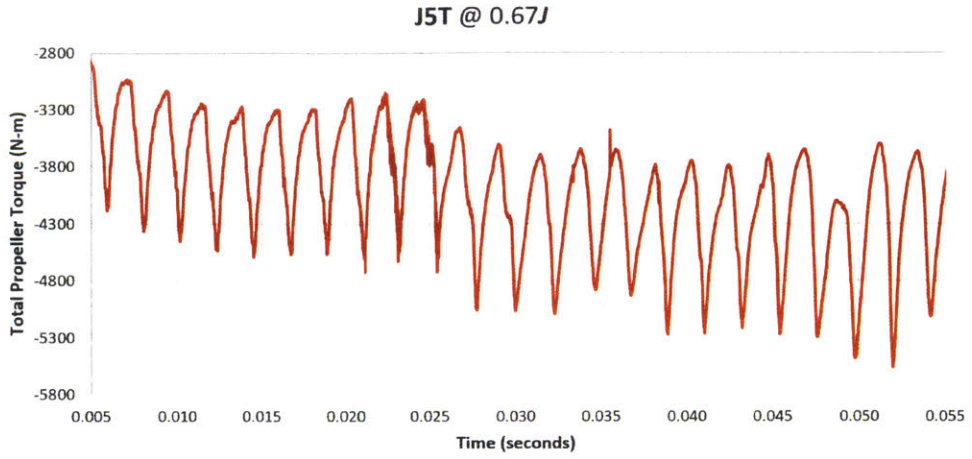

(a) Total torque profile over duration of simulation

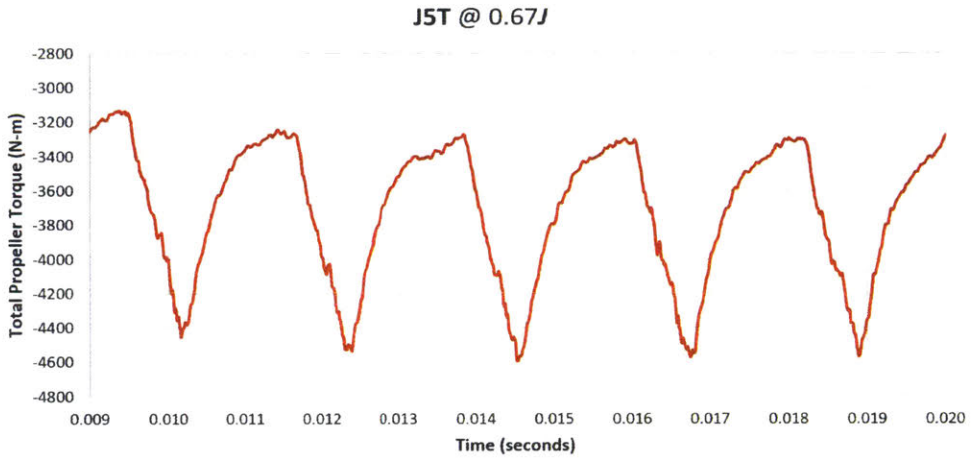

(b) Selected region before discontinuity

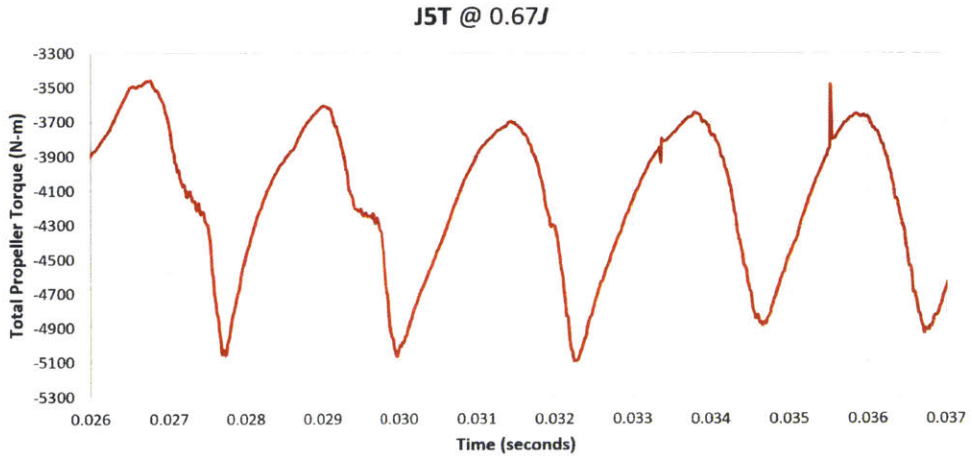

(c) Selected region after discontinuity

Figure 5-23: Total Torque at 2/3 Advance Ratio for *J5T* Propeller

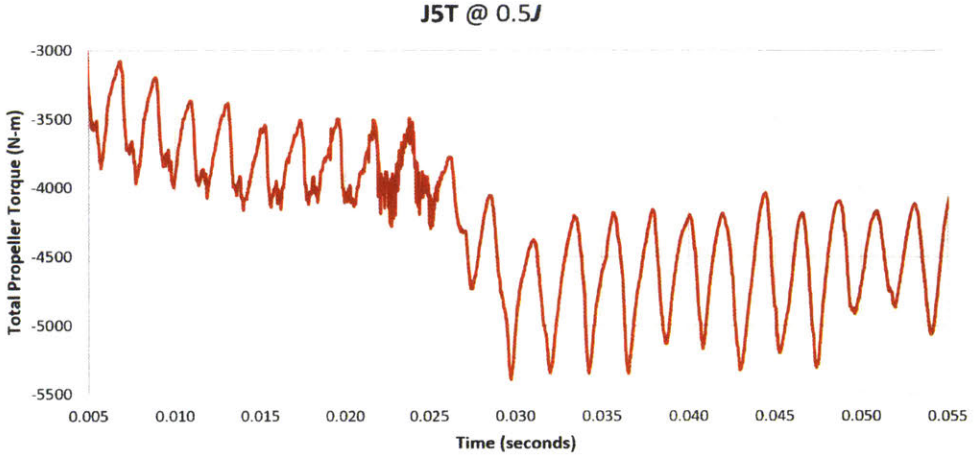

(a) Total torque profile over duration of simulation

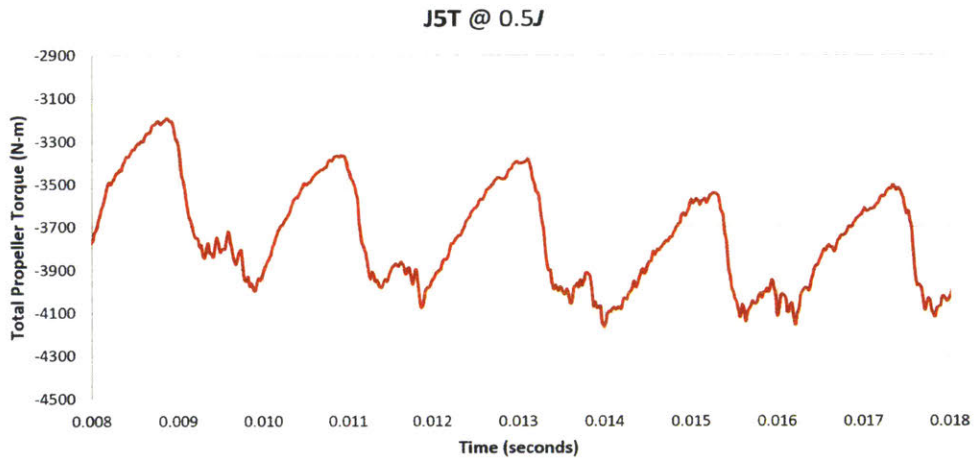

(b) Selected region before discontinuity

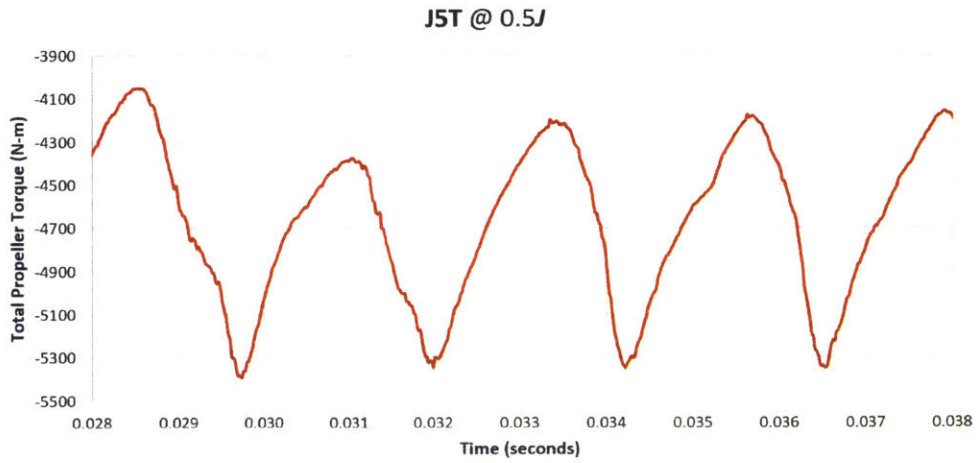

(c) Selected region after discontinuity

Figure 5-24: Total Torque at 1/2 Advance Ratio for *J5T* Propeller

Chapter 6

Conclusion and Recommendations

The design and analysis of the *J5T* propeller ultimately demonstrated a feasible design for high-speed craft. Section 6.1 demonstrates that the performance of the new design is comparable to that of the Mercury baseline. Section 6.2 provides recommendations for future work to further develop this unique propeller concept.

6.1 Assessment of Final Propeller Design

The analysis of the new-design *J5T* propeller shows promising results as compared to its baseline counterpart. From Tables 5.2 and 5.3, the *J5T* is even or slightly superior to the baseline in overall propeller efficiency. These near-equivalent results indicate promise for future improvements, for although this project was unable to benefit from multiple iterations of the propeller design due to time and resource limitations, further iterations to optimize the *J5T* design would very likely be able to improve upon the propeller efficiency.

Figures 6-1 and 6-2 show the final comparison of thrust and torque coefficients at different advance ratios for both propellers. Figure 6-3 compares their ultimate open-water propeller efficiencies. Ideally such graphs - standard in propeller analyses - would have significantly more data points to develop the trend curve. Unfortunately again due to time and resource constraints only six simulations were able to be accomplished. Additional simulations across a greater range of advance ratios would be a highly desirable next step. Nevertheless, the expected curvature of supercavitating propellers is observed in these graphs.

Overall, the *J5T* demonstrates promising performance as a surface-piercing, supercavitating propeller for high-speed watercraft. However, significant additional research is required to attain an optimal design as well as to quantify its full performance spectrum.

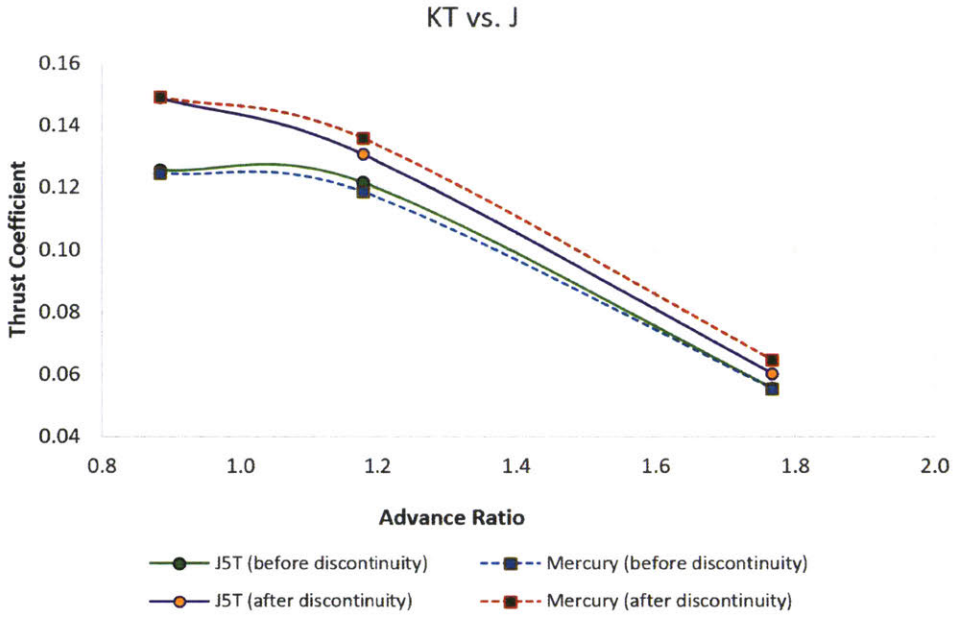

Figure 6-1: Thrust Coefficient vs. Advance Ratio for both propellers

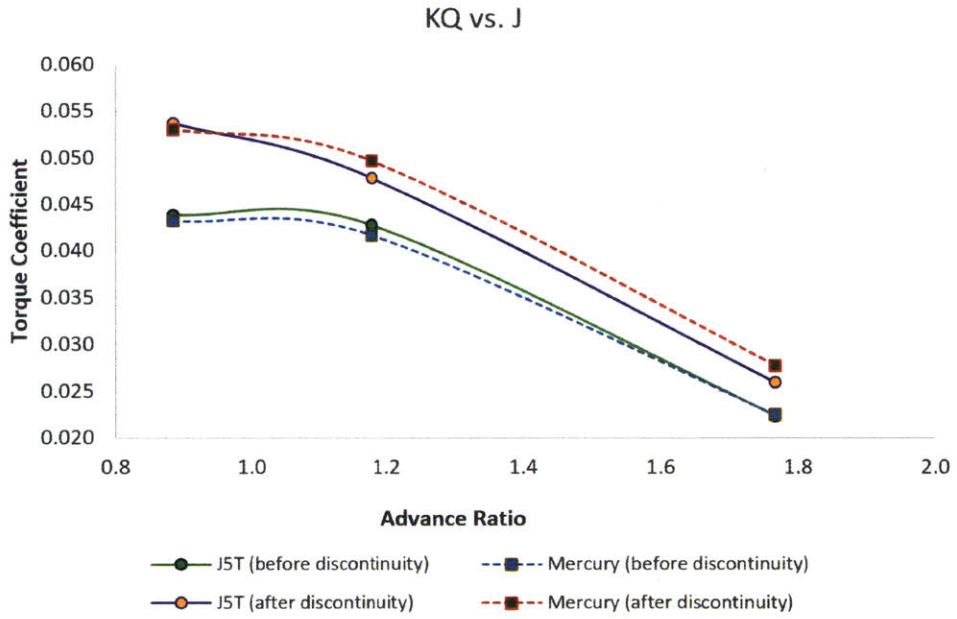

Figure 6-2: Torque Coefficient vs. Advance Ratio for both propellers

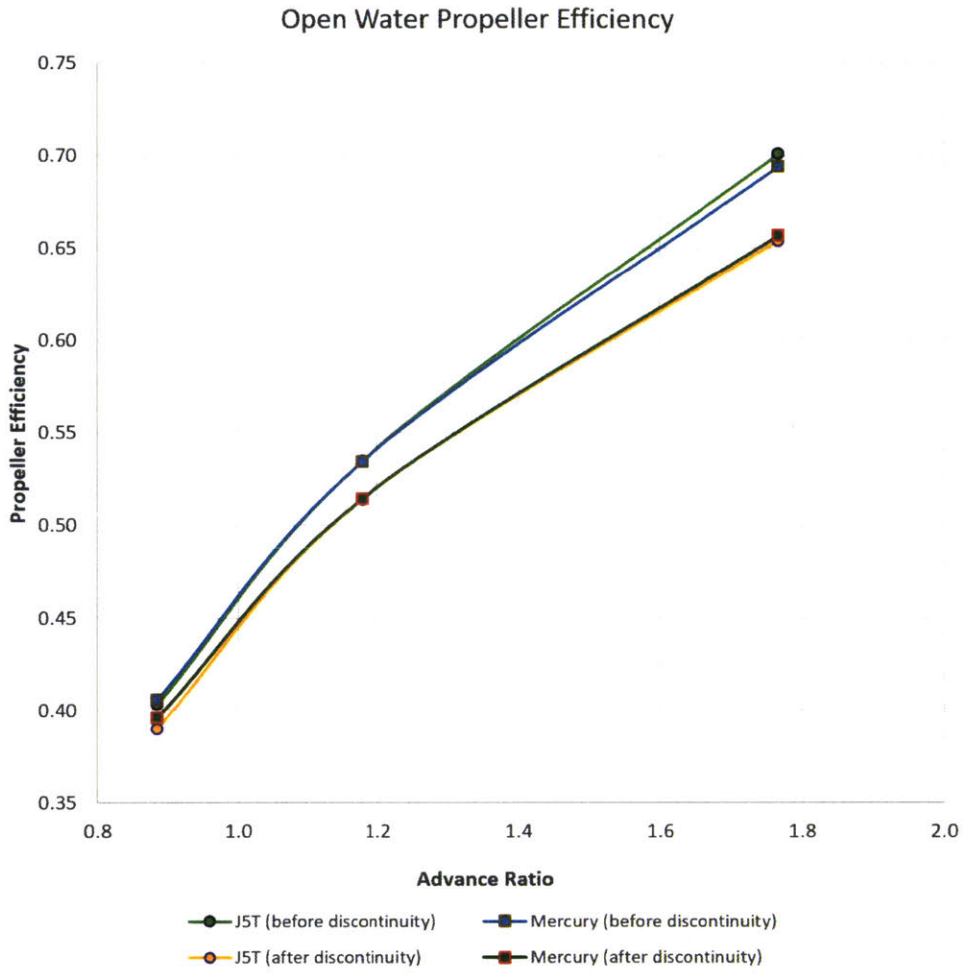

Figure 6-3: Open Water Propeller Efficiency vs. Advance Ratio for both propellers

6.2 Recommendations for Future Work

Significant opportunities for further development of the *J5T* propeller remain. This project initiated the design and analysis of the original, unconventional propeller design, and further work is encouraged to explore its potential. Specifically, the following actions are recommended for the next phase of research:

- Revisit the hydrofoil profile design for further optimization via 2D CFD;
- Rebuild the non-pressure profile geometry, taking further consideration of its effect on the 3D curvature of the full blade;
- Conduct cavitation tunnel testing of the 2D hydrofoils to verify CFD results and inform the design;
- Conduct additional 3D CFD simulations at multiple advance ratios to build detailed performance profiles;
- Conduct full-scale propeller testing, potentially at the Mercury Marine facility.

Finally, for additional propeller research to be conducted at MIT, the author strongly advocates for the restoration of the MIT Cavitation Tunnel (Figure 6-4). Once a world-class facility, this tunnel has unfortunately fallen into disrepair (it was intended for use in this thesis). A complete overhaul of the tunnel to restore it to full operation would allow MIT's proud tradition of naval architecture to continue in the field of high-speed hydrodynamics.

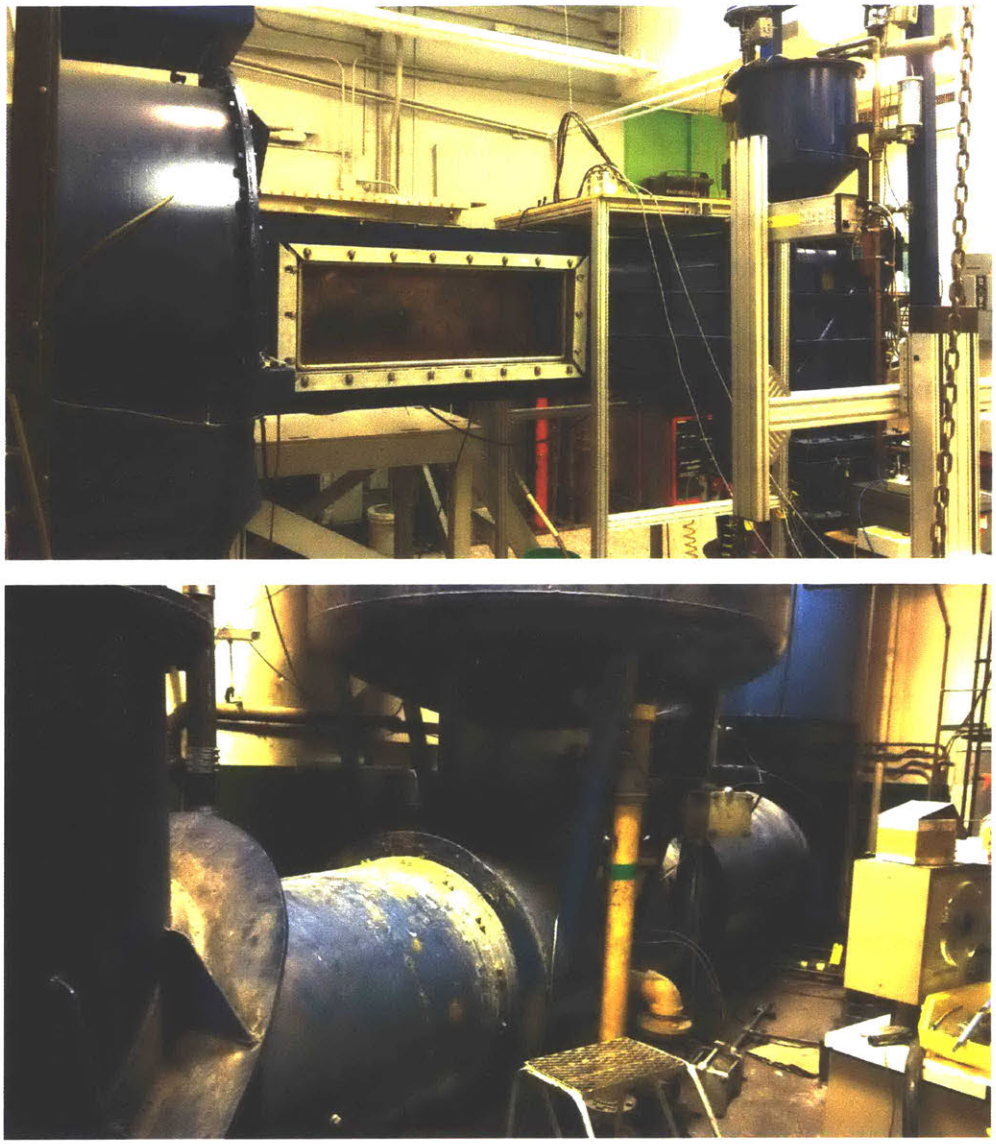

Figure 6-4: MIT cavitation tunnel upper and lower levels

Appendix A

Matlab Code for 3D Geometry

Software: MATLAB version R2017a [23].

Input: Text files containing 2D (x, y) coordinates for each radial profile section, titled "0.15.txt" for the radial section at $r/R = 0.15$ and so forth; manually change **rake** & **skew** scalars and **chord**, **pitch**, & **radius** vectors within code.

Output: Single text file containing 3D coordinates for import into CAD software (e.g. Rhino [27]).

Numbers in code below correspond to the final J5T propeller design, constructed from **eight** radial profile sections.

```
clc; clear all; close all;

Rake = 15; % [deg] Rake (X-Z plane) - constant 15 deg
Skew = 0; % [deg] Skew (Y-Z plane) - no skew
Rake = degtorad(Rake); % [rad] Rake
Skew = degtorad(Skew); % [rad] Skew ("ThetaS")

rVector = [0.0322580 0.0431800 0.0647700 0.1079500 0.1511300
0.1943100 0.2094230 0.2159000]; % [m] Radius vector

cVector = [0.1494316 0.1465051 0.1447800 0.1447800 0.1313153
0.0811602 0.0428183 0.0127000]; % [m] Chord vector
```

```
PitchVector = [79.67028 75.51066 67.76709 54.67500 44.78242
37.45057 35.35275 34.51581]; % [deg] Pitch vector

PitchVector = degtorad(PitchVector); % [rad] Pitch vector

for i = 1:length(rVector)
% Constants for each section
r = rVector(i); % [m] Radius
c = cVector(i); % [m] Chord
Pitch = PitchVector(i); % [rad] Pitch ("ThetaNT")
iG = r*tan(Rake); % [m] Generator Line Rake

% Import x,y points from text files
if i == 1; [x y] = importfile('015.txt');
elseif i == 2; [x y] = importfile('020.txt');
elseif i == 3; [x y] = importfile('030.txt');
elseif i == 4; [x y] = importfile('050.txt');
elseif i == 5; [x y] = importfile('070.txt');
elseif i == 6; [x y] = importfile('090.txt');
elseif i == 7; [x y] = importfile('097.txt');
elseif i == 8; [x y] = importfile('100.txt');
end

% New 3D section definitions
for j = 1:length(x)
xp = -(iG + r*Skew*tan(Pitch)) + x(j)*sin(Pitch) + y(j)*cos(Pitch);
yp = r*sin(Skew - (x(j)*cos(Pitch) - y(j)*sin(Pitch))/r);
zp = r*cos(Skew - (x(j)*cos(Pitch) - y(j)*sin(Pitch))/r);
NewCoords(j + length(x)*(i-1), :)  = [xp yp zp];
end

% Consolidate all new data into new file for Rhino import
dlmwrite('Full-3D-Points.txt', NewCoords, 'delimiter', '\t',
'precision', 10)
end
```

References

[1] Alexander S. Achkinadze. Supercavitating Propellers. Brussels, Belgium, 2001.

[2] Alexander S. Achkinadze. Supercavitating, Highly Cavitating and Surface Piercing Propellers Design. St. Petersburg, Russia, 2005. International Conference on Fast Sea Transportation.

[3] Roderick A. Barr. Supercavitating and Superventilated Propellers. *Transactions of SNAME*, 78:417–450, 1970.

[4] S. Brizzolara and L. Bonfiglio. Comparative CFD Investigation on the Performance of a New Family of Super-Cavitating Hydrofoils. In *Journal of Physics: Conference Series*, volume 656, page 012147. IOP Publishing, 2015. URL: http://iopscience.iop.org/article/10.1088/1742-6596/656/1/012147/meta.

[5] Stefano Brizzolara. A New Family of Dual-Mode Super-Cavitating Hydrofoils. Austin, Texas, United States, 2015. Fourth International Symposium on Marine Propulsors.

[6] Stefano Brizzolara and Alessandro Federici. Super-Cavitating Profiles for Ultra High Speed Hydrofoils: a Hybrid CFD Design Approach. In *Proceedings of the 9th Symposium on High Speed Marine Vehicles*, volume 1, pages 1–13, Naples, Italy, 2011.

[7] Stefano Brizzolara and Diego Villa. Three Phases RANSE Calculations for Surface-Piercing Super-Cavitating Hydrofoils. In *Proceedings of the 8th International Symposium on Cavitation*, pages 13–16, Singapore, August 2012. URL: http://www.academia.edu/download/32730647/CAV2012_SB-DV_v4.2.pdf.

[8] Mario Caponnetto. RANSE Simulations of Surface Piercing Propellers. In *Proceedings of the 6th Numerical Towing Tank Symposium*, 2003. URL: http://www.caponnetto-hueber.com/wp-content/uploads/2016/10/RANSE_Simulations_of_Surface_Piercing_Propellers_NUTTS_2003.pdf.

[9] John S. Carlton. *Marine Propellers and Propulsion.* Butterworth-Heinemann, Oxford, 2nd edition, 2007. OCLC: 255583388.

[10] Dennis J. Clark, William M. Ellsworth, and John R. Meyer. The Quest for Speed at Sea. *Technical Digest, Naval Surface Warfare Center, Carderock Division*, 2004. URL: http://foils.org/02_Papers%20dnloads/041115NSWCTD_QuestSpeed.pdf.

[11] Enbao Ding. A Series of Surface Piercing Propellers and Its Application. Shanghai, China, September 2007.

[12] Marco Ferrando, Stefano Crotti, and Michele Viviani. Performance of a Family of Surface Piercing Propellers. In *Proceedings of the 2nd International Conference on Marine Research and Transportation*, Naples, Italy, June 2007.

[13] Jordan Golson. How We Can Get Submarines to Travel at Supersonic Speed, August 2014. URL: https://www.wired.com/2014/08/how-we-can-get-submarines-to-travel-at-supersonic-speed/.

[14] J. L. Hwang, S. Y. Wang, J. S. Kouh, W. S. Wang, and T.C. Yeh. Design, Manufacture and Full Scale Trial of High Performance Surface-Piercing Propeller. Technical report, 1999.

[15] Virgil E. Johnson. Theoretical and Experimental Investigation of Supercavitating Hydrofoils Operating Near the Free Water Surface. Technical R-93, Langley Research Center, Langley Field, Virginia, United States, 1961.

[16] Juliet Marine Systems. Juliet Marine //. URL: http://www.julietmarine.com/.

[17] Joseph Katz and Allen Plotkin. *Low-Speed Aerodynamics: From Wing Theory to Panel Methods*. McGraw-Hill series in aeronautical and aerospace engineering. McGraw-Hill, New York, 1991.

[18] Richard W. Kimball. *2D Mast/Sail Foil Experiment*. PhD thesis, Massachusetts Institute of Technology, Cambridge, Massachusetts, United States, May 1997.

[19] Spyros A. Kinnas. Supercavitating 3-D Hydrofoils and Propellers: Prediction of Performance and Design. Brussels, Belgium, 2001. URL: http://oai.dtic.mil/oai/oai?verb=getRecord&metadataPrefix=html&identifier=ADP012091.

[20] Spyros A. Kinnas and C. H. Mazel. Numerical Versus Experimental Cavitation Tunnel (A Supercavitating Hydrofoil Experiment). *Journal of Fluids Engineering*, 115(4):760–765, 1993. URL: http://fluidsengineering.asmedigitalcollection.asme.org/article.aspx?articleid=1427647.

[21] Michael Klesius. The Department of Never Mind. *Air & Space Magazine*, September 2009. URL: http://www.airspacemag.com/history-of-flight/the-department-of-never-mind-39415310/.

[22] Claus F. L. Kruppa. High Speed Propellers Hydrodynamics and Design. Technical report, University of Michigan, September 1969.

[23] MathWorks. MATLAB, February 2017. URL: https://www.mathworks.com/.

[24] Kyle Mizokami. "Supercavitation" Could Let Submarines Move Ridiculously Fast, June 2016. URL: http://www.popularmechanics.com/military/research/a21572/supercavitation-penn-state-research-submarines/.

[25] Anthony F. Molland and Stephen R. Turnock. *Marine Rudders and Control Surfaces: Principles, Data, Design and Applications.* Elsevier/Butterworth-Heinemann, Amsterdam ; London, 2007. OCLC: ocn137222335.

[26] Niclas Olofsson. *Force and Flow Characteristics of a Partially Submerged Propeller.* PhD thesis, Chalmers University of Technology, Goteborg, Sweden, 1996.

[27] Robert McNeel & Associates. Rhinoceros, September 2016. URL: https://www.rhino3d.com/.

[28] John C. Rose, Claus F. L. Kruppa, and Kourosh Koushan. Surface Piercing Propellers - Propeller/Hull Interaction. Yokohama, Japan, 1993.

[29] San Francisco Maritime National Historical Park (U.S. National Park Service). Agitation?? No...Cavitation!! URL: https://www.nps.gov/safr/learn/historyculture/propsaquaticpark.htm.

[30] J. Sauer and G. H. Schnerr. Unsteady Cavitating Flow âĂŞ a New Cavitation Model Based on a Modified Front Capturing Method and Bubble Dynamics. In *Proceedings of 2000 ASME Fluid Engineering Summer Conference*, pages 11–15, Boston, MA, June 2000. URL: https://www.researchgate.net/profile/Guenter_Schnerr_Professor_Dr-Inghabil/publication/295743779_Unsteady_cavitating_flow_-_A_new_cavitation_model_based_on_a_modified_front_capturing_method_and_bubble_dynamics/links/57ab7a5b08ae7a6420bfa3ce.pdf.

[31] J. O. Scherer, J. Bohn, and R. Altmann. The Design of Supercavitating Propellers. Technical report, Hydronautics, Inc., August 1976.

[32] John Scherer. Propeller Definition for Prototype Design, July 2015.

[33] Siemens. STAR-CCM+, April 2017. URL: https://thesteveportal.plm.automation.siemens.com/.

[34] A. J. Tachmindji and W. B. Morgan. The Design and Estimated Performance of a Series of Supercavitating Propellers. Technical report, 1959.

[35] Marshall P. Tulin and Roderick A. Barr. On The Range of Applicability of Supercavitating and Ventilated Propellers. Technical 134-1, Hydronautics, Inc., September 1961.

[36] Marshall P. Tulin and M.P. Burkart. Linearized Theory for Flows About Lifting Foils at Zero Cavitation Number. Technical Report C-638, David W. Taylor Model Basin, February 1955.

[37] Giuliano Vernengo and Stefano Brizzolara. A Reformulated Lifting Line Theory for Supercavitating Hydrofoil Design. In *Proceedings of the 8th International Symposium on Cavitation*, Singapore, 2012.

[38] William S. Vorus. Forces on Surface-Piercing Propellers with Inclination. *Journal of Ship Research*, 35(3):210–218, September 1991.

[39] Y. Young and S. Kinnas. Numerical Analysis of Surface-Piercing Propellers. In *2003 Propeller and Shaft Symposium*, pages 4–1 – 4–20, 2003.